

REPORT DOCUMENTATION PAGE			Form Approved OMB No. 0704-0188		
The public reporting burden for this collection of information is estimated to average 1 hour per response, including the time for reviewing instructions, searching existing data sources, gathering and maintaining the data needed, and completing and reviewing the collection of information. Send comments regarding this burden estimate or any other aspect of this collection of information, including suggestions for reducing the burden, to the Department of Defense, Executive Service Directorate (0704-0188). Respondents should be aware that notwithstanding any other provision of law, no person shall be subject to any penalty for failing to comply with a collection of information if it does not display a currently valid OMB control number.					
<b>PLEASE DO NOT RETURN YOUR FORM TO THE ABOVE ORGANIZATION.</b>					
1. REPORT DATE (DD-MM-YYYY) 30-09-2011		2. REPORT TYPE FINAL		3. DATES COVERED (From - To) July 2008 - June 2011	
4. TITLE AND SUBTITLE Mechanics of Granular Materials: Experimentation and Simulations for Determining the Compressive and Shear Behaviors of Sand at Granular and Meso Scales			5a. CONTRACT NUMBER		
			5b. GRANT NUMBER FA9550-08-1-0328		
			5c. PROGRAM ELEMENT NUMBER		
6. AUTHOR(S) Subramanian, Vijay and Luo, Huiyang and Wang, Fang and Cooper, William, L, and Lu, Hongbing and Komanduri, Ranga			5d. PROJECT NUMBER		
			5e. TASK NUMBER		
			5f. WORK UNIT NUMBER		
7. PERFORMING ORGANIZATION NAME(S) AND ADDRESS(ES) Oklahoma State University School of Mechanical and Aerospace Engineering 218 Engineering North Stillwater, OK 74078			8. PERFORMING ORGANIZATION REPORT NUMBER		
9. SPONSORING/MONITORING AGENCY NAME(S) AND ADDRESS(ES) Air Force Office of Scientific Research 875 N. Randolph Street Arlington, VA 22203-1768			10. SPONSOR/MONITOR'S ACRONYM(S) AFOSR		
			11. SPONSOR/MONITOR'S REPORT NUMBER(S) AFRL-OSR-VA-TR-2012-0268		
12. DISTRIBUTION/AVAILABILITY STATEMENT Approved for Public Release; Distribution is Unlimited.					
13. SUPPLEMENTARY NOTES					
14. ABSTRACT We present the results of experiments conducted to study the compressive and shear behavior of sand. Static and dynamic studies on the compression of sand grains were conducted. Nanoindentation was performed on single grains on sand of different sizes in order to determine the elastic and fracture properties of individual sand grains. Finite Element method (FEM) was used to solve the inverse problem so as to obtain the material properties from the load-displacement curves obtained from nanoindentation experiments. We also report the results of quasi-static compression tests conducted on sand held in a passive confinement. An in-house built compression fixture enabled the compression of sand grains up to axial stresses as high as 3 GPa. The results of tests conducted to study the dynamic behavior of ensemble to sand grains to compressive loading are also presented. Dynamic compression tests at strain rates of ~700 1/s were performed using a split Hopkinson pressure bar (SHPB). Characterization of sand grains based on initial packaging density, moisture content and different confinement materials were performed. In-situ quasi-static compression of sand grains along with X-ray micro-computed tomography was performed.					
15. SUBJECT TERMS Granular Materials, Eglin Sand, Mechanical Behavior of Sand, Nanoindentation, Split Hopkinson Pressure Bar (SHPB), micro-CT					
16. SECURITY CLASSIFICATION OF:			17. LIMITATION OF ABSTRACT UU	18. NUMBER OF PAGES 83	19a. NAME OF RESPONSIBLE PERSON Vijay Subramanian
a. REPORT U	b. ABSTRACT U	c. THIS PAGE U			19b. TELEPHONE NUMBER (Include area code) 405-334-1104

# **AFOSR FINAL REPORT**

## **Principal Investigators:**

Ranga Komanduri  
A. H. Nelson, Jr. Endowed Chair in Engineering  
OSU Regents Professor  
Oklahoma State University  
School of Mechanical and Aerospace Engineering  
218 Engineering North  
Stillwater, OK 74078  
Phone: (405) 744-5900

Hongbing Lu  
Louis Beecherl Jr. Chair  
Professor of Mechanical Engineering  
University of Texas at Dallas  
ECSN 2.528  
800 West Campbell Rd  
Richardson, TX 75080-3021  
Phone: (972) 883-4647

## **Title:**

Mechanics of Granular Materials: Experimentation and Simulations for Determining the Compressive and Shear Behaviors of Sand at Granular and Meso Scales

## **Grant Number:**

FA9550-08-1-0328

## **Grant Period:**

July 1, 2008 - June 30, 2011

## **Abstract**

We present the results of experiments conducted to study the compressive and shear behavior of sand. Static and dynamic studies on the compression of sand grains were conducted. Nanoindentation was performed on single grains on sand of different sizes in order to determine the elastic and fracture properties of individual sand grains. Finite Element method (FEM) was used to solve the inverse problem so as to obtain the material properties from the load-displacement curves obtained from nanoindentation experiments. We also report the results of quasi-static compression tests conducted on sand held in a passive confinement. An in-house built compression fixture enabled the compression of sand grains up to axial stresses as high as 3 GPa. The results of tests conducted to study the dynamic behavior of ensemble to sand grains to compressive loading are also presented. Dynamic compression tests at strain rates of  $\sim 700 \text{ s}^{-1}$  were performed using a split Hopkinson pressure bar (SHPB). Characterization of sand grains based on initial packaging density, moisture content and different confinement materials were performed. In-situ quasi-static compression of sand grains along with X-ray micro-computed tomography was performed. Images from the tomographs were combined with the axial stress-strain data to explain various phenomenon such as re-arrangement and eventual fracture of grains during compression. Results obtained from various experiments performed in the course of this study would serve to validate the analytical models on mechanical behavior of sand.

## **Introduction**

Granular or particulate materials are ensembles of discrete macroscopic particles that respond to external forces only via inter-particle contact forces. They resemble solids as they behave rigidly under compression due to grain interlocking. Due to discrete and unbonded nature of the grains, they cannot withstand any load under tension. When the interlocking between the grains collapse, they lose resistance to shear loading and exhibit flow behavior similar to that of a viscous fluid. The solid-liquid transitional behavior of

the granular materials can be observed in grains stored in silos to landslides. They resemble liquids by assuming the shape of the container that they are stored and resemble gases as they lack intergranular cohesion. Jaeger *et al.* describe granular materials as “unusual” solids, liquids or gases [31]. They describe granular materials as a unique state of matter. The study of granular materials is currently active in various fields of engineering and sciences; including physics, geophysics, mechanics, and pharmaceuticals. Sand is a granular material found abundantly in nature. It has a hard structure with particle size varying between  $7.5 \mu\text{m}$  and  $4.75 \text{ mm}$ . It primarily consists of silica ( $\text{SiO}_2$ ) while other constituents, such as magnetite, gypsum, chlorite are present in minor quantities and vary from one geographic location to the other. Sand is usually described by their composition, morphology (shape), size, color, and texture.

Among many applications such as for use as a construction material, and as a raw material for glass and silicon, sand is often used to provide ballistic protection for military structures. Understanding the mechanical behavior of sand is also important to investigate the interaction of blast wave induced by improvised explosive devices with military vehicles and personnel, as well as earthquakes and landslides. It is well known that dense sand has high compressive strength and high energy absorption capacity. In recent years, there is a growing interest in the investigation of the mechanical behavior of sand, partially due to the advent of advanced instrumentation (e.g., nanoindentation, pulse-shaped Kolsky bar) and the high-performance inexpensive parallel computer (e.g., cluster), which enable much larger grain ensembles to be considered. While numerous publications exist on the mechanical behavior of bulk sand for geological and civil engineering applications, the focus has been on the mechanical behavior at low stress levels and quasi-static compression under confinement [23, 62]. For applications involving high speed impact of an object with sand, the statistically-varied mechanical behavior of individual sand grains under high stress has to be understood. Under such a condition, a fundamental understanding of the underlying mechanisms of deformation, flow, and fracture of granular materials under load, is needed to investigate the mechanical behavior at mesoscale and

continuum scale. Ultimately, it can be used to explain the large scale phenomena such as sand penetration, and the shearing and sliding during earthquakes and landslides.

The mesoscale behavior of sand depends strongly on the mechanical behavior of individual sand grains. For this purpose it is particularly important to determine the mechanical properties such as the Young's modulus, hardness, fracture toughness, and constitutive law for sand grains. Moreover, the mechanical properties of the grains can change due to changes with the mineral composition, size, defects and crystal structure in sand grains. The larger grains may contain defects in the form of voids, ridges and cracks, yielding mechanical properties different from the smaller grain sizes [17]. The small sand grains usually stay at the top layers and may be affected more by wind and chemicals it carries. The large sand grains usually settle at the bottom, and may affect more by pressure, which cause possibly different crystal structures and mechanical properties of sand grains with different sizes.

Many efforts have been made on characterizing the mechanical behavior of sand, through experiments such as compression [4, 19, 32, 46], shear [28, 61], and stress wave propagation [22, 42]. For understanding the mechanical behavior at mesoscale it is necessary to determine the mechanical properties of individual sand grains for applications in geomechanics and particulate mechanics simulations. However, due to the small size, it is difficult to carry the conventional tensile, compressive or shear experiments on individual small sand grains to determine the mechanical properties. Therefore, nanoindentation becomes an effective tool to characterize the mechanical properties of sand grains.

## Chapter 1

# Characterization of Eglin Sand

The sand used in this investigation was quartz sand ( Quikrete #1961 sand quarried in Pensacola, FL) ASTM D2487 [1] standard was used to conduct the particle size analysis. The procedure for particle size analysis involves screening of oven-dried sand through a series of stacked sieves of decreasing mesh size in a mechanical shaker (Dual Mfg. Co., Model # D-4326) Eleven sieves were used in this analysis. Figure 1.1 show the cumulative plot of % mass of sand passing through each sieve against the corresponding sieve size. The values of  $D_{10}$  and  $D_{60}$  are obtained from the grain size distribution plot.  $D_{10}$  and  $D_{60}$  are the diameters of sand grains for which 10% and 60% of the particles are finer, respectively. The co-efficient of uniformity,  $C_U = \frac{D_{60}}{D_{10}}$ , was calculated to be 2.13.  $C_U$  value of less than 4 indicates uniform particle size, as is the case with Eglin sand. Poorly graded sands have a steep size distribution curve. Based on Unified Soil Classification system (USCS), Eglin sand is categorized as SP-SM. The symbol ‘S’ represents Sand, ‘SP-SM’ refers to poorly graded sand with silt. Table 1.1 summarizes the physical properties of Eglin sand obtained from sieve analysis and from the survey of the literature [58].

Transmission electron microscopy (JEOL 2100F TEM/STEM operating at 200 kV) was used to characterize the micro-structure of an Eglin sand grain. TEM samples were prepared using a focused ion beam (FIB) apparatus (FEI Nova NanoLab 200). The bright field TEM images, including the selected area electron diffraction patterns (Figure 1.2) clearly show two-layer structure in an Eglin sand grain: amorphous layer on the outer

Table 1.1: Physical Properties of Eglin sand from particle size analysis.

USCS Classification	SP-SM
Specific Gravity	2.65 (reported by [58])
$D_{50}$ or Average grain size	0.375 mm
$D_{60}$ Particle Size	0.420 mm
$D_{10}$ Particle Size	0.197 mm
Uniformity, $C_U = \frac{D_{60}}{D_{10}}$	2.13

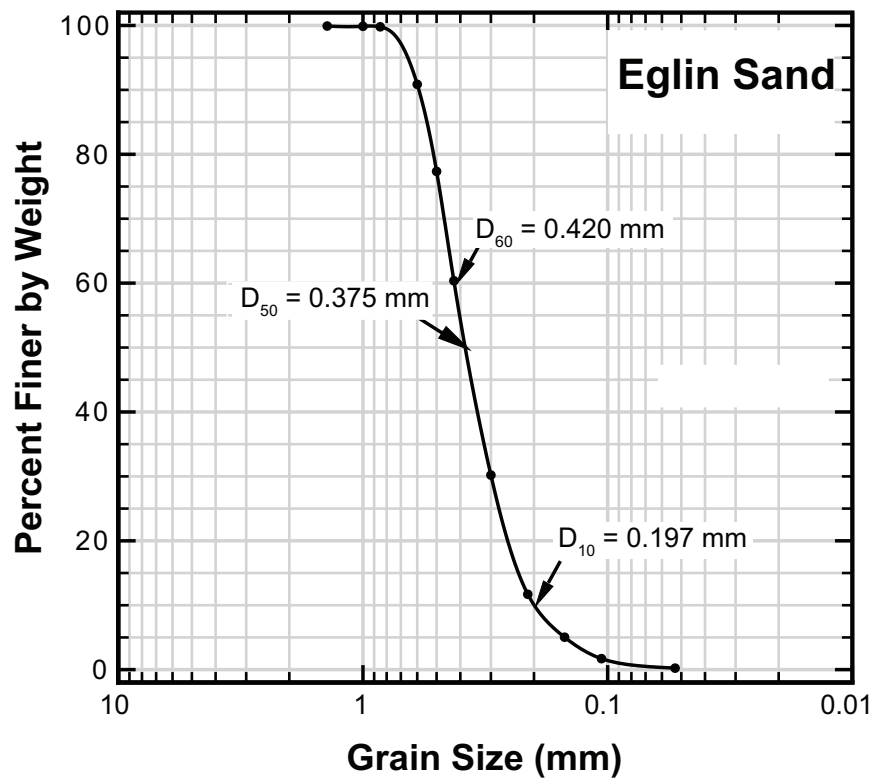
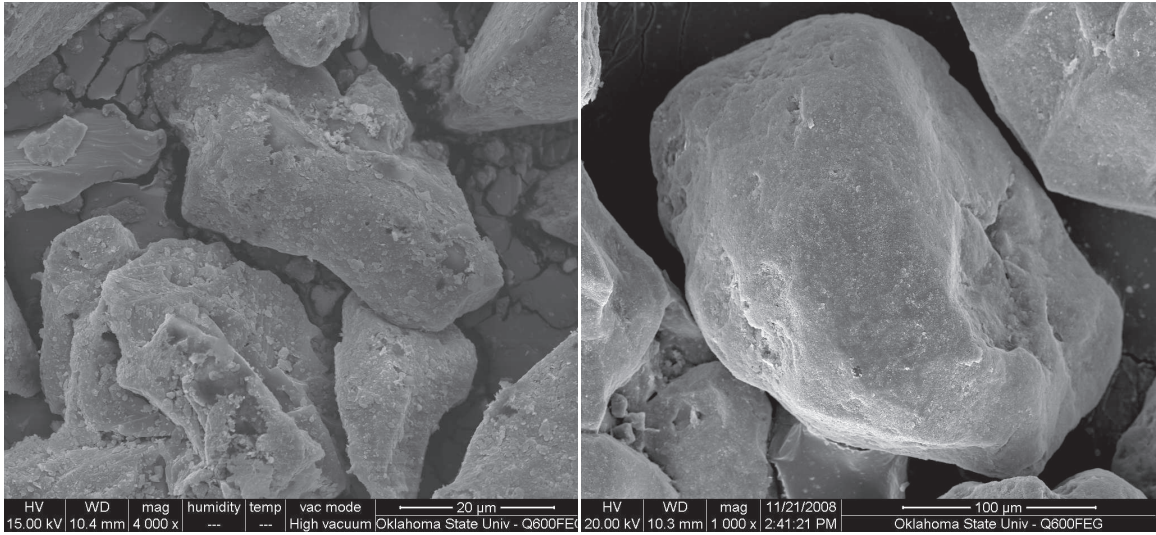
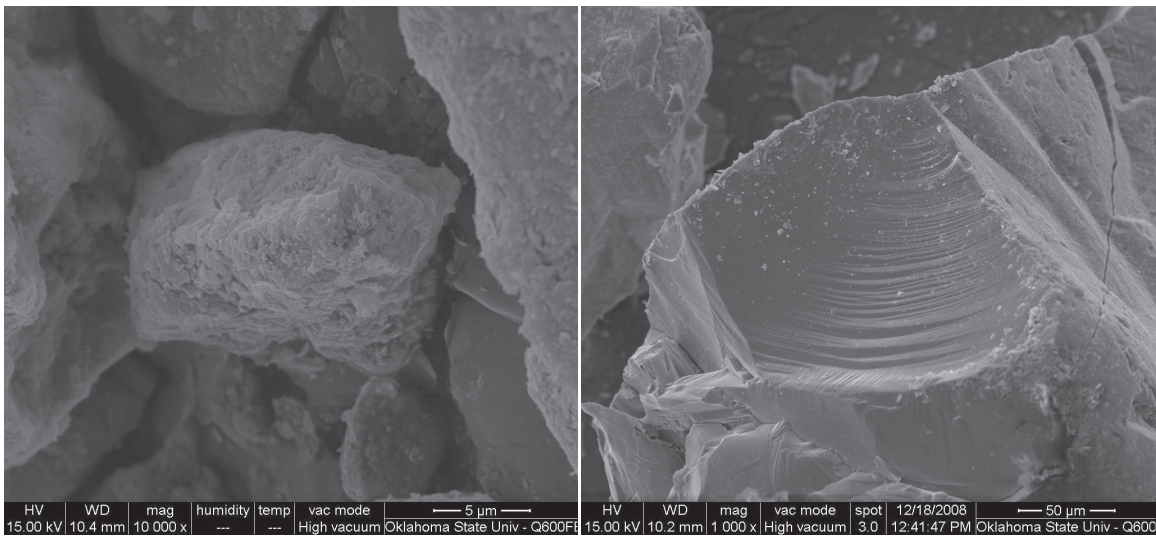


Figure 1.1: Sieve analysis for determining particle size distribution of Eglin sand. The steep curve indicates a somewhat poorly graded sand.



(a)

(b)



(c)

(d)

Figure 1.2: SEM images of sand grains at various magnifications showing grain shapes, rounded edges and surface features such as cracks and pits, fracture akin to glass fracture.

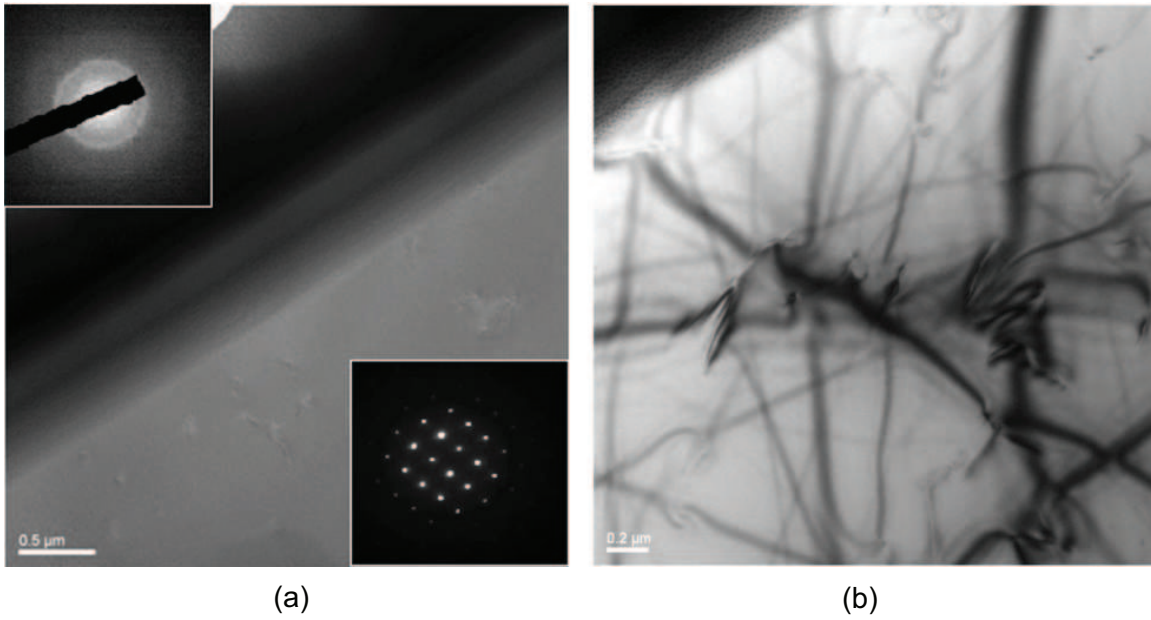


Figure 1.3: TEM images of Eglin sand grain (a) Bright field image showing two layers with different diffraction patterns; (b) Bright field image showing dislocation in the interior layer.

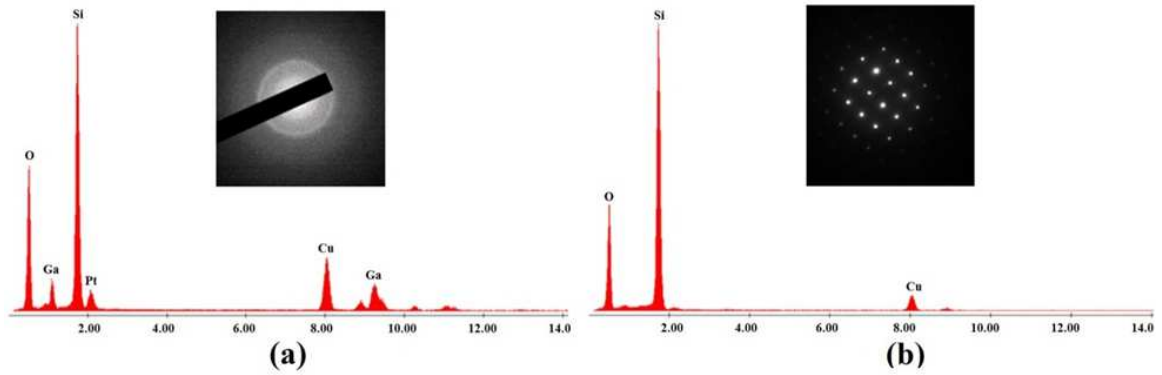


Figure 1.4: EDS and electron diffraction patterns of Eglin sand grains (a) Amorphous outer layer; (b) Crystalline interior layer.

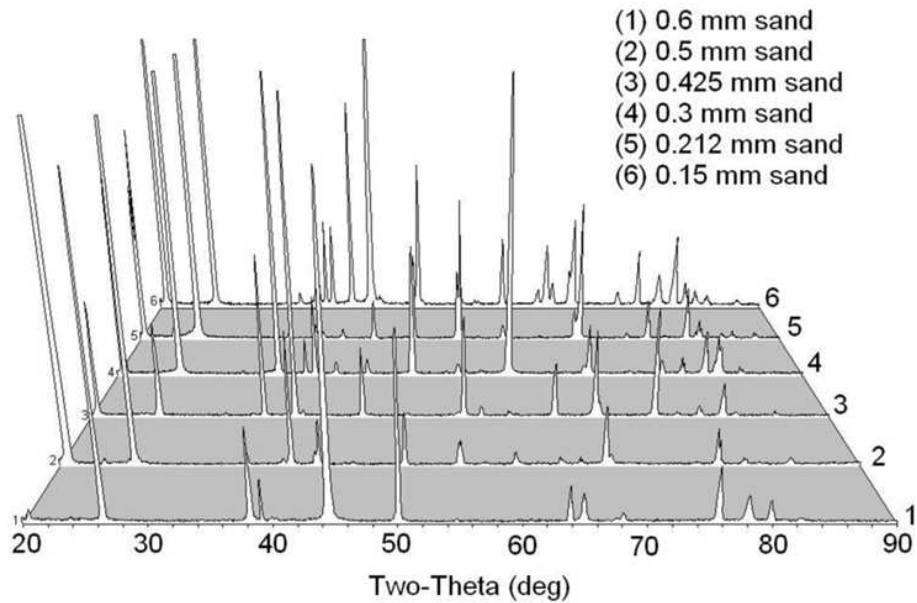


Figure 1.5: X-ray diffraction patterns of Eglin sand grains.

layer and crystalline interior layer. Dislocations or other possible crystal structural defects are also observed in the interior layer as shown in the TEM image (Figure 1.3).

The EDS spectra in Figure 1.4 show presence of silicon and oxygen in their oxide compounds in a sand grain. It is noted that the Ga signal is from the FIB Ga ion beam, Pt signal from the Pt coating used to prepare TEM samples, and Cu signal from the grid used to support the TEM sample, which are related to the sample preparation, not associated with the elements of sand. There are some differences in the chemical constituents between the amorphous outer surface (Figure 1.4(a)) and crystalline interior (Figure 1.4(b)). It appears that the outer amorphous layer contains a bit more oxygen than the inner crystalline layer, in consideration of the oxygen/silicon ratio. EDS results show that the Eglin sand consisted primarily of silica quartz with the presence of small amounts of other chemical elements, which may contribute to the variation of mechanical properties.

XRD (Rigaku Ultima III X-ray Diffractometer) were conducted on sand

grains with different sizes, to assess their crystalline structure. The XRD diffraction patterns (intensity vs  $2\theta$ ) of six sizes of sand grain samples are shown in Figure 1.5. Since the sand grain samples are randomly selected, the intensity values may vary for different batches. Most of the diffraction peak angles are the same, confirming the EDS results showing that the sand is primarily silica. There are, however, some differences between these six patterns, which indicate that sand grains with different sizes may have slightly different structures, different material constituents, and defects, etc. Comparing sand diffraction data with the database maintained by the International Center for Diffraction Data, it is found that most of the sand grain patterns match reasonably well with the  $\alpha$ -quartz diffraction pattern. Since the structures and chemical constituents of Eglin sand vary with the grain size, nanoindentation tests were conducted on different sizes of sand to determine how the properties change with grain size.

## Chapter 2

# Nanoindentation Tests on Sand Grains

*This study was conducted by Fang Wang and Nitin Daphalapurkar at Oklahoma State University. The details of this study are documented elsewhere [17,60].*

For each of the six sizes, the sorted sand grains were embedded in an epoxy matrix in a sample holder. The samples were cured in an oven at 50°C for 24 hours, resulting in a composite of sand grains in a hardened epoxy matrix. The samples were wet-polished using alumina abrasive slurry (Buehler Inc., Minneapolis, MN) on a rotating polishing wheel covered with a cloth pad. To obtain a smooth surface suitable for nanoindentation, the minimum abrasive size used in the final polishing was 50 nm. After polishing, the sand sample surfaces were cleaned by acetone to remove any remaining epoxy that may cover sand grain surfaces. Subsequently, alcohol was used to remove remaining acetone to prevent it from eroding the supporting epoxy.

An MTS Nano Indenter XP system was used for the nanoindentation measurements. This indenter can reach a maximum indentation depth of 500  $\mu\text{m}$  (resolutions 0.2 nm) and a maximum load of 500 mN (resolutions 50 nN). Both Berkovich and cube-corner indenter tips, made of single crystal diamond, were used in this investigation. Nanoindentations were made on horizontally flat, polished sand grain surfaces under constant rate loading. The vertically applied load on the indenter tip was increased until it reached a user-defined value, followed by unloading. The load-displacement curves

were analyzed to determine the mechanical properties of the sand grains based on the contact mechanics analysis of nanoindentation. The hardness ( $H$ ) is obtained using

$$H = \frac{P_{max}}{A_c} \quad (2.1)$$

where  $P_{max}$  is the maximum indentation force,  $A_c$  is the contact area corresponding to the contact depth ( $h_c$ ) at the maximum load, which is calculated based on the tip area function. To determine the modulus of the specimen, the reduced modulus of the specimen ( $E_r$ ) is calculated at first using

$$\frac{1}{E_r} = \frac{1 - \nu_s^2}{E_s} + \frac{1 - \nu_i^2}{E_i} \quad (2.2)$$

where  $E_s$  and  $\nu_s$  are the Young's modulus and Poisson's ratio of the specimen, respectively, and  $E_i$  and  $\nu_i$  are the Young's modulus and Poisson's ratio of the indenter tip (made up of diamond), respectively. Due to finite stiffness of the indenter tip, its modulus is considered in the calculation of sand grain modulus from the contact stiffness. The contact stiffness ( $S$ ) is calculated from the slope of the initial unloading curve,

$$S = \frac{dP}{dh} = \frac{2}{\sqrt{\pi}} E_r \sqrt{A_c h_c} \quad (2.3)$$

Equations (2.2) and (2.3) along with the known values of the area function of the nanoindenter tip, the indent depth, the slope of the unloading curve, and the Young's modulus and Poisson's ratio values for the indenter tip were used to determine the elastic modulus for a specimen.

## 2.1 Young's Modulus and Hardness of Sand Grains

For the measurement of Young's modulus and hardness, an indentation force was applied by the nanoindenter using a Berkovich tip on a sand grain. Each test was conducted near the center of a sand grain to minimize the edge effect. The Young's modulus was determined from the slope of the unloading curve using Equation (2.2), and the hardness was calculated from the peak load and the corresponding contact area with Equation (2.1). These were the direct outputs from the nanoindentation software, based

on Equation (2.1) and (2.3). We first carried out nanoindentation tests on a relatively large (around 0.7 mm) sand grain. Young's modulus and a Hardness of  $72.4 \pm 2.8$  GPa and  $11.2 \pm 0.7$  GPa were obtained from 10 tests on several grains with different orientations. When indentation carried out on the same grain we kept a distance of at least  $50 \mu\text{m}$  between neighboring indents. For the same grain the Young's modulus values are consistent when nanoindentation was made on the same surface, indicating homogeneous behavior on the same grain.

For nanoindentation conducted on different grains the mechanical properties determined for nearly 0.7 mm sand grains have very small uncertainty (within a range of 5%). The percent weight of 0.7 mm grains or larger is less than 5%. For the next six sizes of sand grains, one test was conducted on each sand grain. Figure 2.1(a) shows a typical nanoindentation residual impression and Figure 2.1(b) shows a typical inverted image (3D) obtained using MTS NanoVision. The inverted image (Figure 2.1(b)) enables the determination of the depth of the indent with convenience and delineates its topographical features. Figure 8 shows a typical nanoindentation load-displacement curves for 0.425 mm sand grains (at  $P_{50}$  value). It is seen that the loading-displacement curves for larger size grains (0.600 mm, 0.500 mm and 0.425 mm) nearly overlap with each other while the curves show variation for smaller sand grains (0.300 mm, 0.212 mm and 0.150 mm). For nanoindentation measurements on these six samples, the distribution of Young's modulus and hardness will be analyzed to determine the statistical results.

The Weibull distribution is one of the most widely used distribution functions and was found appropriate to describe the distribution of the mechanical properties for sand grains. The Weibull plot of statistical distributions of the Young's modulus and the hardness values are shown in Figures 4.9 and 4.10, respectively. The curves show that most data points fall on a straight line, indicating that these properties follow the Weibull distribution. The

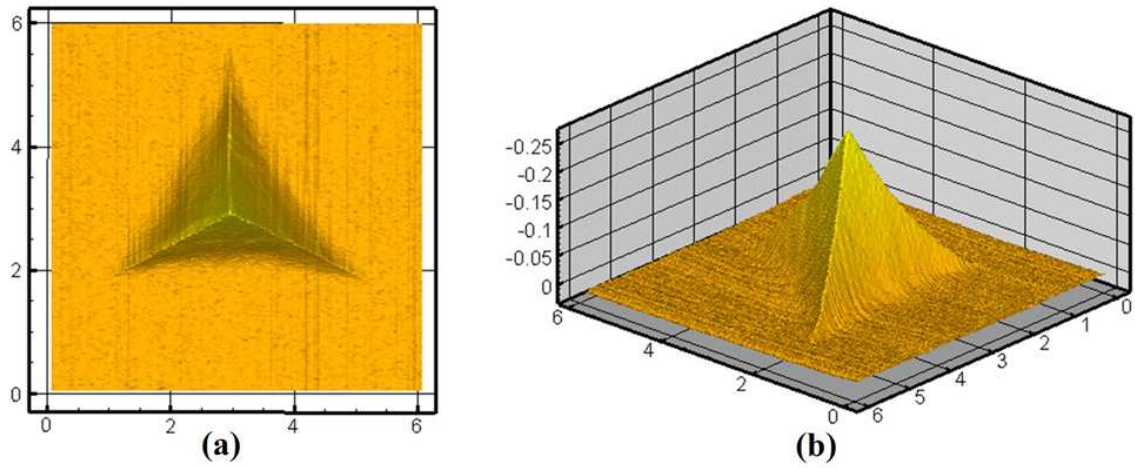


Figure 2.1: Typical indent image on a sand grain using Berkovich tip (a) 2D residual indent impression; (b) 3D inverted indent image (dimensions in  $\mu\text{m}$ ).

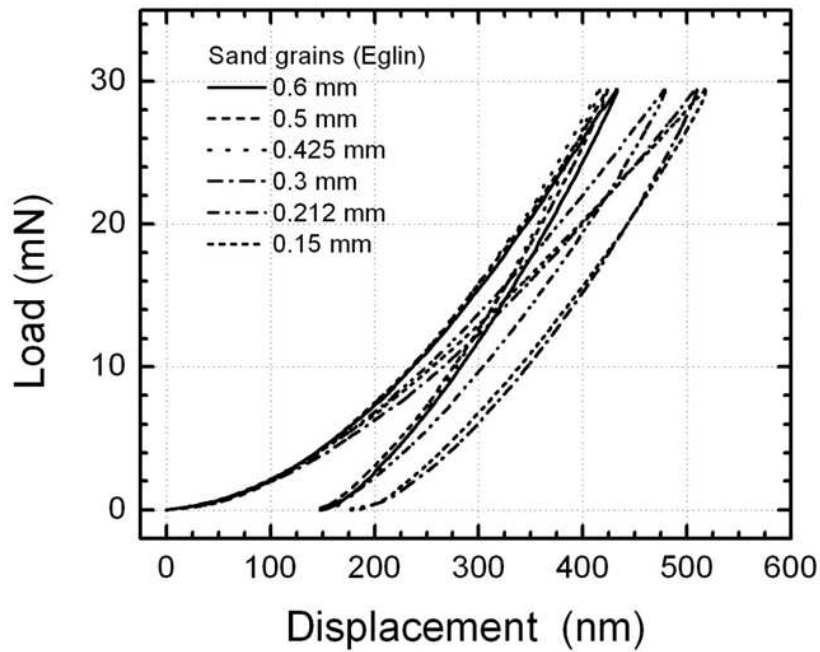


Figure 2.2:  $P_{50}$  nanoindentation load-displacement curves for six sizes of sand grains under Berkovich tip.

Weibull probability distribution function is given by

$$f(x) = \frac{k}{\lambda} \left(\frac{x}{\lambda}\right)^{k-1} e^{-\left(\frac{x}{\lambda}\right)^k}, 0 \leq x \leq +\infty \quad (2.4)$$

where  $k > 0$  is the shape parameter and  $\lambda > 0$  is the scale parameter of the distribution. Its complementary cumulative distribution function is a stretched exponential function given as

$$F(x) = 1 - e^{-\left(\frac{x}{\lambda}\right)^k} \quad (2.5)$$

where  $x \geq 0$  and  $F(x) = 0$  for  $x < 0$ . The Weibull plot is a diagram of the empirical cumulative distribution function of data plotted using  $\ln(x)$  as abscissa and  $\ln(-\ln(1 - F(x)))$  as ordinate. If the relationship follows a straight line, then the data follows Weibull distribution.

The Weibull plot of statistical distributions of the Young's modulus and the hardness values are shown in Figures 2.3 and 2.4, respectively. The curves show that most data points fall on a straight line, indicating that these properties follow the Weibull distribution. Larger sand grains in general have relatively higher Young's moduli and hardness values. A closer examination indicates that as sand grains become smaller from 0.600, 0.500 and 0.425 mm, the  $P_{30}$  Young's modulus values increase from 97.4 GPa, to 102.1 GPa and 108.9 GPa, respectively. As the grain sizes reduce further, the  $P_{30}$  Young's modulus values become 80.8 GPa, 77.5 GPa, and 71.5 GPa for grain sizes 0.300 mm, 0.210 mm and 0.150 mm, respectively. The  $P_{50}$  Young's modulus values show similar trend. The maximum Young's modulus is attained at sand size of 0.425 mm, which is the median grain size of the Eglin sand. Similarly for hardness of the six grain sizes, the  $P_{50}$  hardness values reach the highest value at the median grain size (0.425 mm). It is noted that the Young's modulus values are not coincident with those in different crystallographic orientations of single crystal quartz. There are several possible reasons. The crystal orientations of larger and smaller grains may be different.

From XRD results (Figure 1.5), differences among the diffraction patterns indicate the differences in structures of sand grains of various sizes. The Young's moduli of X-cut, Y-cut and Z-cut of single crystal quartz reported are 79 GPa, 79 GPa and 103 GPa respectively [12]. The nanoindentation results on different 0.6 mm grains shows 97.4 GPa modulus, indicating orientation independent properties. As a result, sand grains are most likely polycrystalline. It is noted that the amorphous layer of sand grains should have Young's modulus around 70 GPa (fused silica). Amorphous layer constitutes higher volume fraction of small Eglin sand grains than on larger ones. A possible reason for small modulus observed in small grains might be the epoxy effect. To examine this, we conducted FEM simulation for a small sand (0.15 mm) grain on an epoxy substrate. The results indicate that the epoxy effect is negligible. However, after polishing, some sand grains might be very thin especially for smaller grains because a portion of the grain was removed during the polishing. In this case, the epoxy underneath could affect the nanoindentation results. As shown in Figure 2.3, for smaller sand grains, there are several small Young's modulus values (less than 40 GPa) which could be induced by the effect of epoxy layer, with a Young's modulus on the order of around 3 GPa. Further, the material constituents and defect structural differences can be possible reasons for difference in property data as well. Combining the nanoindentation results of all sand grains with six sizes together, the Weibull distribution for Young's moduli and hardness for assorted as-received Eglin sand are determined, as shown in Figures 2.5(a) and 2.6(a), respectively. From Figures 2.5(b) and 2.6(b), the overall Young's moduli for the Eglin sand grains are found to be 90.4 GPa (with a range from 33.4 to 119.8 GPa), hardness to be 12.8 GPa (range 4.2 to 20.3 GPa) while larger sand grains having relatively higher values and smaller sand grains having relatively lower values.

## 2.2 Stress-strain Relationship of Eglin Sand Grains

The methods used for extracting Young's modulus from nanoindentation have been well established. Inverse methodologies, which use experimentation in combination with numerical simulations to aid in characterizing

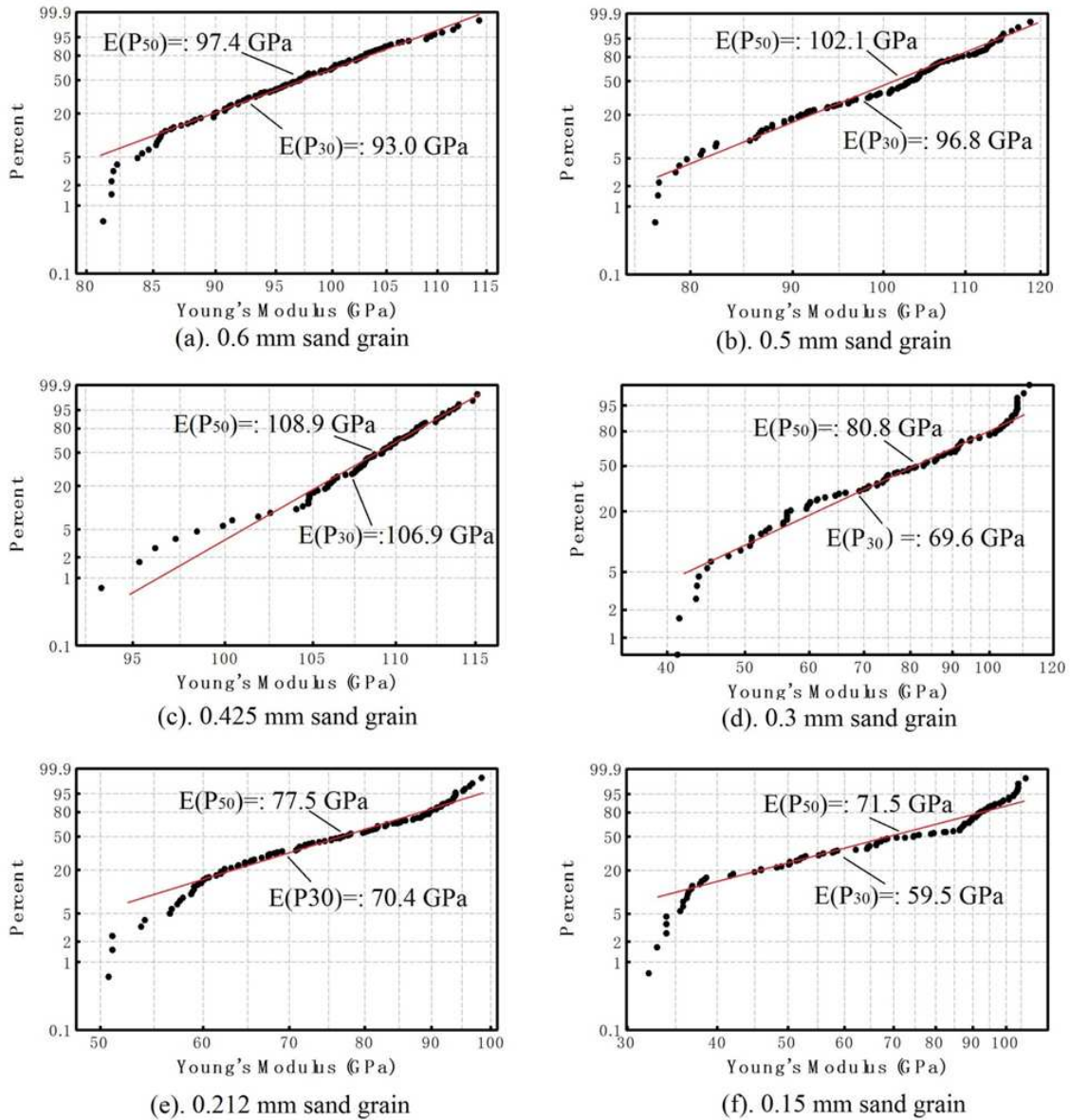


Figure 2.3: Weibull plots of Young's modulus from nanoindentation on six different sizes of sand grains. (a) 0.6 mm; (b) 0.5mm; (c) 0.425 mm; (d) 0.3mm; (e) 0.212 mm; (f) 0.15 mm.

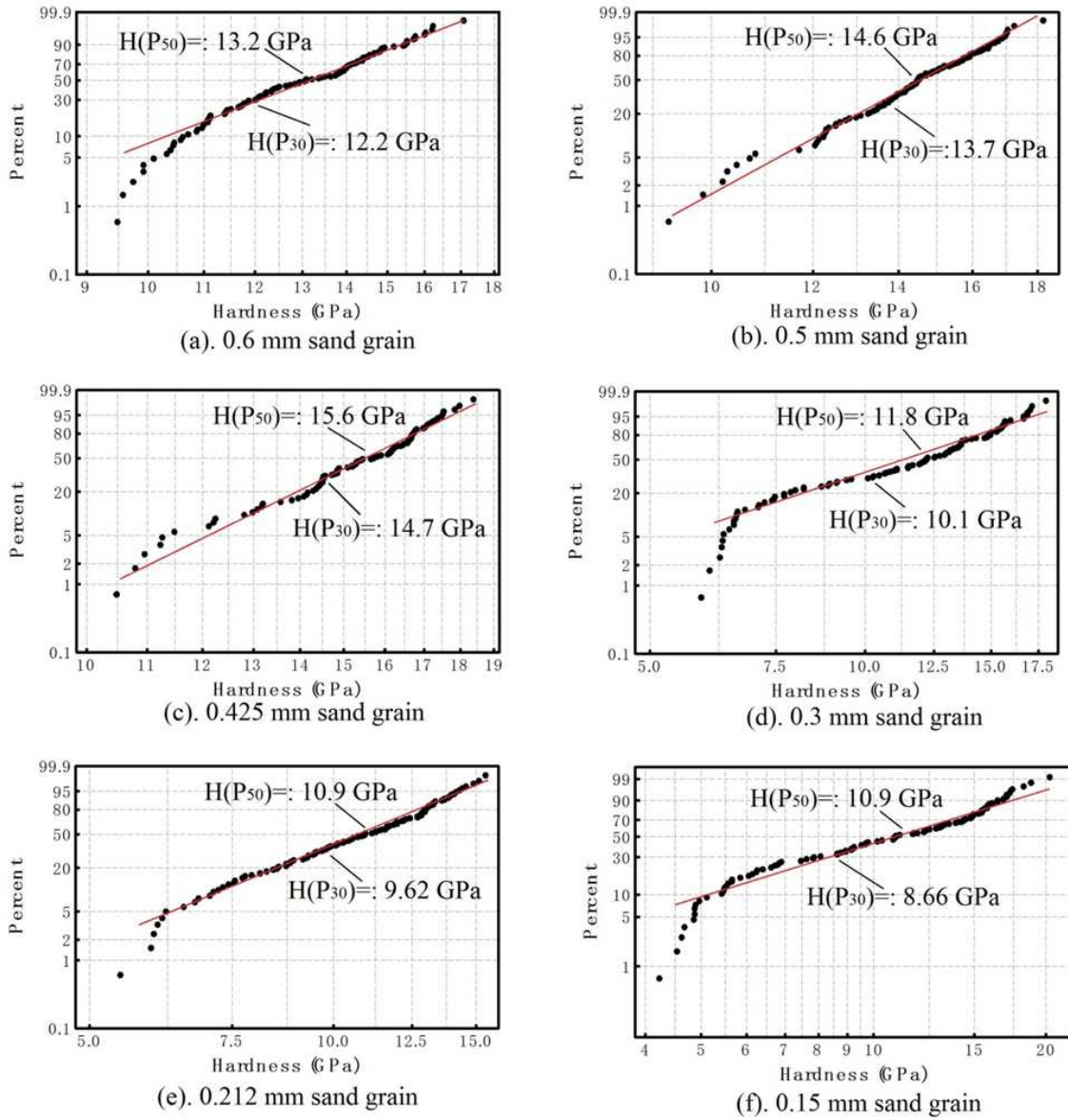


Figure 2.4: Weibull plots of nanoindentation hardness from nanoindentation on six sizes of sand grains. (a) 0.6 mm; (b) 0.5mm; (c) 0.425 mm; (d) 0.3mm; (e) 0.212 mm; (f) 0.15 mm.

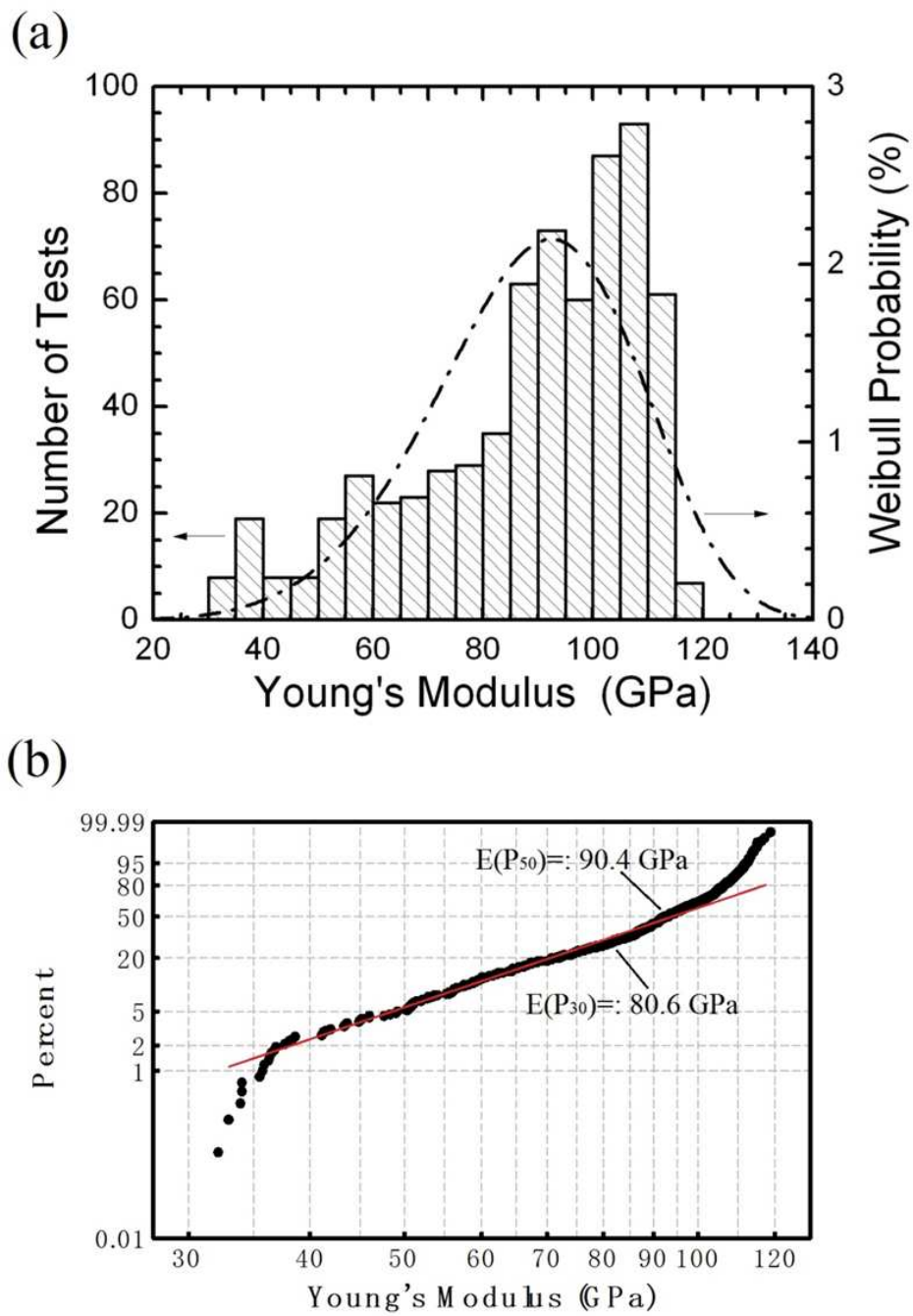


Figure 2.5: Statistical results of Young's modulus results from nanoindentation for assorted sand grains of all sizes. (a) Weibull distribution; (b) Weibull plot.

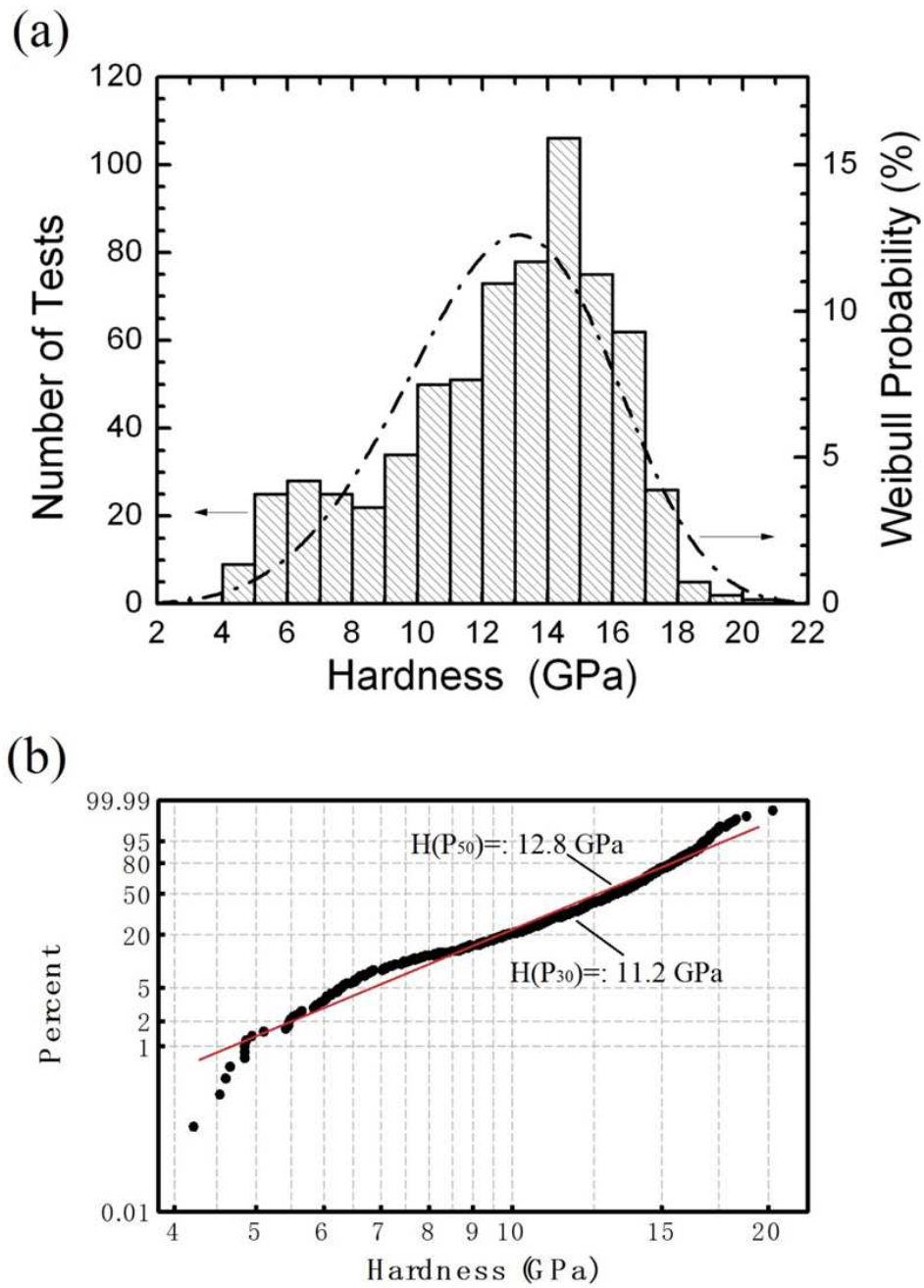


Figure 2.6: Statistical results of nanoindentation hardness for assorted sand grains of all sizes. (a) Weibull distribution; (b) Weibull plot.

the material properties, are used when it is difficult to extract material properties due to nonlinearities or complexity of material, geometry, and loading conditions. FEM has been used successfully in the simulations of similar nanoindentation problems [6, 7]. In such cases, it is necessary to simulate the indentation of an indenter tip in an elastic-plastic half space. In general, nominal constitutive parameters are assumed, and then adjusted so that numerical results agree with the experimental values. In this case, the experimental and numerical load/unloading-displacement curves in the nanoindentation are compared.

To determine the elastic-plastic properties, von Mises yield criterion was used along with isotropic hardening to simulate the deformation characteristics of a sand grain. The plastic behavior under compression was assumed to follow the power law in form of Ramberg-Osgood relationship. For isotropic materials, the multidimensional Ramberg-Osgood model is expressed as the strain components  $\epsilon_{ij}$  as a function of the stress components  $\sigma_{ij}$  as

$$\epsilon_{ij} = \frac{1}{E}[(1 + \nu)\sigma_{ij} - \nu\delta_{ij}\sigma_{kk}] + \frac{3}{2}\alpha \left(\frac{\sigma_e}{\sigma_y}\right)^{(n-1)} \frac{S_{ij}}{E} \quad (2.6)$$

where  $\alpha$  is the yield offset and  $n$  is the hardening exponent,  $\sigma_y$  is the yield stress,  $\nu$  is Poisson's ratio and  $E$  is Young's modulus.  $\delta_{ij}$  is Kronecker delta (1 when  $i=j$ , and 0 when  $i \neq j$ ,  $i, j = 1, 2, 3$ ),  $\sigma_e$  is the Mises equivalent stress defined as  $\sigma_e = \sqrt{\frac{3}{2}S_{ij}S_{ij}}$ ,  $S_{ij}$  is the Cauchy stress deviator given as  $S_{ij} = \sigma_{ij} - \frac{1}{3}\sigma_{kk}$ , where  $\sigma_{kk}$  is the principal components of stress tensor. In the Equation (2.6), the first term represents the linear elastic Hooke's constitutive law, and the second term is the result of the power-law plastic flow normal to the Miss stress potential. In the uniaxial case (one-dimensional stress status), the Ramberg-Osgood model is simplified as

$$\epsilon = \frac{\sigma}{E} + \alpha \frac{\sigma_y}{E} \left(\frac{\sigma}{\sigma_y}\right)^n \quad (2.7)$$

For modeling quartz in individual sand grains, the stress at 0.2% offset  $\sigma_{0.2}$  is considered as the yield stress  $\sigma_y$ , defined as  $\sigma_y = 0.002\frac{E}{\alpha}$ . In Ramberg-

Osgood model, only three parameters are independent.

In this work, ABAQUS v6.8-3 standard was used in simulations, assuming finite deformation characteristics. A more efficient method was conceived to overcome the time-consuming problems in randomly choosing the parameter, to accelerate the optimizing process. The inverse methodology proposed by Shim *et al.* [50] can be used to extract the stress-strain curve of a single grain crystal materials from FEM simulation of the nanoindentation data. Their work is based on a relationship between hardness and flow stress first provided by Tabor [53] as shown in Equation (2.7)

$$H = C_{\theta}\sigma_f \quad (2.8)$$

where  $C_{\theta}$  is the “constraint factor” depending on the angle,  $\theta$ , of the indenter and flow stress is a characteristic value of plastic strain. The characteristic strain,  $\epsilon_c$ , can be obtained for a given indenter angle. There have been several efforts to obtain the stress-strain curve by relating the hardness to stress and the indenter angle to characteristic strain. Combing Equations (2.7) and (2.8), the hardness can be expressed as a function of  $E$ ,  $\sigma_y$ ,  $C_{\theta}$  and  $\epsilon_c$ ,

$$\log H = n \log \left( \frac{E}{\sigma_y} \epsilon_c \right) + \log(C_{\theta}\sigma_y) \quad (2.9)$$

where the unknown values are only exponent  $n$  and yield stress  $\sigma_y$  for a given indenter angle. In this work, finite element simulation is used to solve the inverse problem to obtain the values of  $n$  and  $\sigma_y$  for the different size Eglin sand grains. Young’s modulus,  $E$ , and hardness,  $H$ , can be measured from nanoindentation experiments. As mentioned previously, nanoindentation simulation results may be affected by parameters coupling, but based on Equation (2.9) the two unknown parameters depend on each other for estimation. Therefore, if one parameter was given, the other value can be estimated using Equation (2.9) directly. In this case, only one parameter is estimated for the model’s input and effect of parameter coupling between yield stress and exponent has been considered.

The model for FEM simulation of nanoindentation is shown in Figure 2.7.

The Berkovich indenter was simulated based on its three sided pyramidal geometry. Due to the three-fold symmetry, only one sixth of the entire model is used in this simulation to reduce the computational time. The displacement history from the experiment was given as input to the FEM analysis. We assume Poisson's ratio (for silica quartz) of 0.18 for all sand grains. The different yield stress values were used to calculate the exponent value for the power law equation which is the input for the plastic behavior of sand. The output of the FEM analysis was the resulting nanoindentation load. This numerical load was plotted versus the displacement into the surface, to generate load-displacement curve from the simulation. The mesh size selected was tested for convergence of the load-displacement curve. In this work, there were 1,646,381 C3D4 (brick) elements used to mesh the sand. By changing the yield stress values for different grain size of the samples and comparing the simulation output with the experimental results until a reasonably good agreement was reached, the two unknown material parameters,  $n$  and  $\sigma_y$  were carefully adjusted until the best-fit results appear. Then the best-fit parameters were used to determine the effective stress-strain relationship for the Eglin sand grains. Although the Young's modulus and hardness values were obtained from the nanoindentation experiments directly, they were also adjusted to match the load-displacement curves from simulations with the experimental curves. However, the adjustment range is limited within 5% of the experimental results.

In this approach, the maximum strain (up to which the stress-strain curve is valid) is limited by the strain produced by the nanoindentation test. Examination of the indent impressions (for the Berkovich indenter tip) obtained from NanoVision indicates that no cracks were formed in nanoindentation using the Berkovich tip. Thus, the continuum plasticity material model is justified. An inverse problem solving approach was used to determine the stress-strain relationship of sand at granular level by correlating the FEM simulated nanoindentation load-displacement data with the measured results. Figure 2.7 shows the simulation results obtained using the inverse problem solving approach to the nanoindentation  $P_{50}$  data for six different grain size samples. It indicates that the simulation results agree reasonably

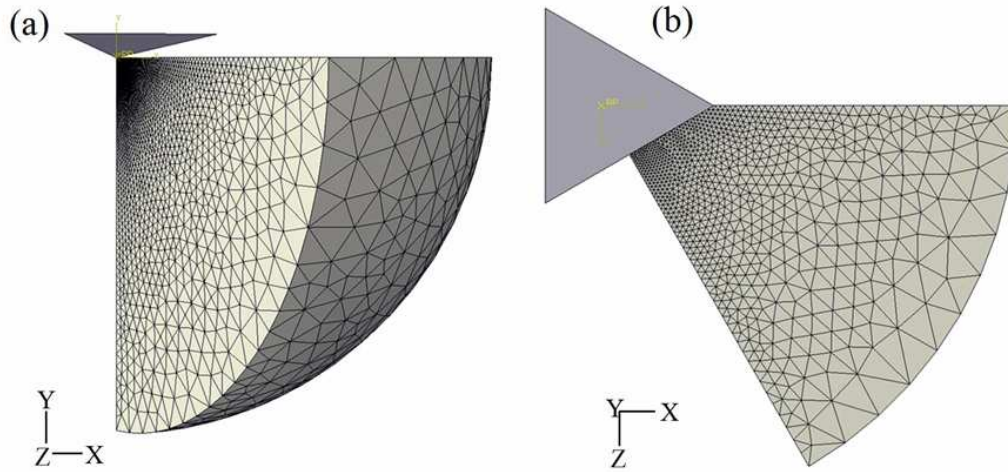


Figure 2.7: Finite Element Analysis model for nanoindentation on 1/6 spherical sand grain using Berkovich tip. (a) Side view of the model. (b) Top view of the model.

well with the experimental results. For the six different size samples, the values for yield stress and exponent of power law equation are about 4.5 - 7 GPa and 2.44 - 4.69 GPa, respectively, using  $P_{50}$  load-displacement curves. These values, together with the measured Young's modulus values can be used as the material parameters for the elastic-plastic constitutive model for Eglin sand grains. The compressive stress-strain curves for six sizes of sand grain obtained by FEM simulation are shown in Figure 2.9. Since the maximum compressive strain in simulation is 35%, the compressive strain in Figure 2.9 is chosen as 35%. It is noted that the curve for larger size sand grains (0.600 mm, 0.500 mm and 0.425 mm) were very close, stiffer than those of the smaller size sand grains (0.300 mm and 0.212 mm), and the weakest is the smallest sand grain of 0.150 mm size.

### 2.3 Parameter Sensitivity in Simulation

Several parameters (Young's modulus, hardness and yield stress) were adjusted to fit the simulated load-displacement curves with the experiment data. As shown in Equation (2.9), the power law index  $n$ , is related with Young's modulus, hardness and yield stress. In order to detect the parameter sensitivity of the simulation model, several series of parameters were assumed and the corresponding simulations were conducted. At

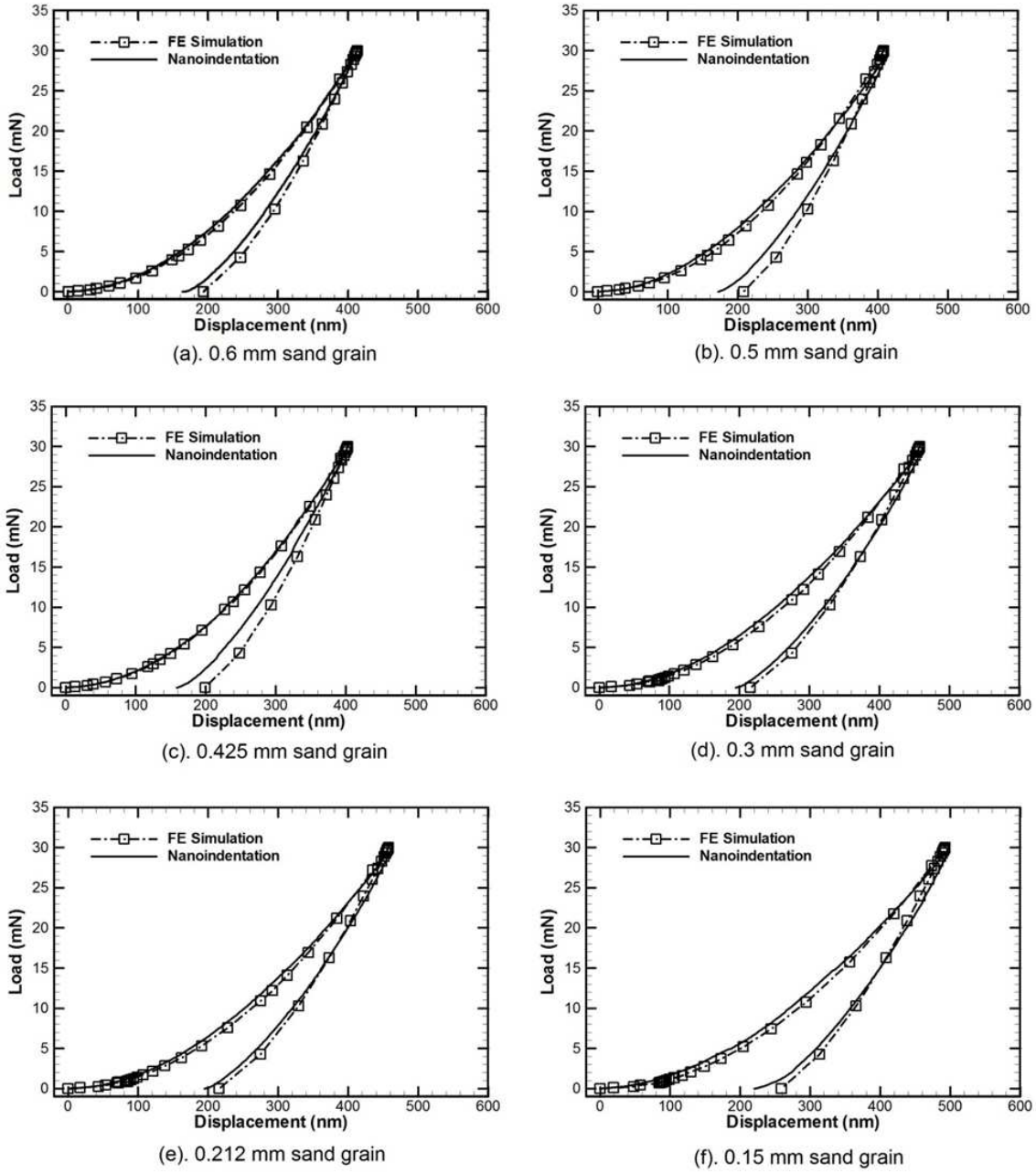


Figure 2.8: Comparison of experimental and simulation results for six grains. (a) 0.600 mm; (b) 0.500 mm; (c) 0.425 mm; (d) 0.300 mm; (e) 0.212 mm; (f) 0.150 mm.

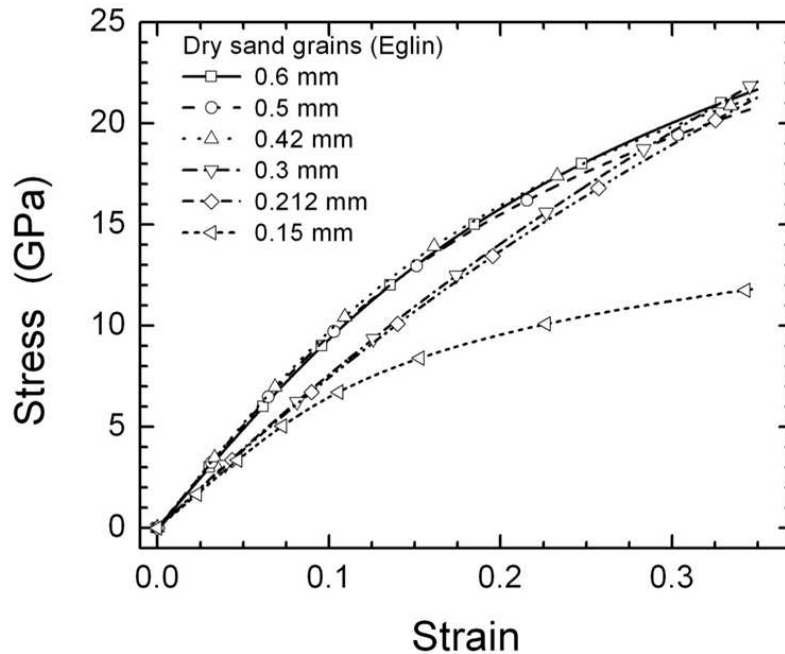


Figure 2.9: Stress-strain relationships of different sizes of Eglin sand grains from the FEM simulations.

first, the Young's modulus values were changed from 2% -10% of the experimental results with other parameters unchanged. The corresponding load-displacement curves did not change very much except for 2% at initial unloading portion. However, the corresponding stress-strain curves can change by 24% at 40% compressive strain level. If the hardness values changed 2%-10%, the stress-strain curves calculated will change for almost 36% at 40% compressive strain level while the load-displacement curves change 2.3% at the initial unloading portion, which indicate that the nanoindentation simulation model is very sensitive to Young's modulus and hardness. However, nanoindentation can measure both Young's modulus and hardness very accurately, typically with 95% of accuracy, so that the effects of Young's modulus and hardness can be minimized. In addition to Young's modulus and hardness, the effect of yield stress was analyzed as well. If the yield stress values change for 20% while other parameters remaining the same, the stress-strain curves will change for 5% at 40%

compressive strain level, which means that the model is less sensitive to yield stress. In this case, the Young's modulus and hardness value adjustment is limited within 5% of the experimental results and the yield stress is the main parameter for fitting the model.

## 2.4 Sand Crystal Structure

The method developed by Oliver and Pharr [43, 44], in general, is not suitable for materials with anisotropic properties [8]. However, the XRD results (Figure 1.5) show that the Eglin sand grains have the same characteristic feature as single crystal  $\alpha$ -quartz, which has a rhombohedral structure. To explore the effect of anisotropy on indentation, a series of nanoindentation experiments on single crystal quartz along different crystal orientations were conducted. The single crystal  $\alpha$ -quartz samples were indented on Z-cut plane [(0001) direction] and X-cut plane [(2 $\bar{1}$ 10) plane]. The Young's Moduli, determined using Oliver and Pharr's analysis are 331 GPa on Z-cut surface, and 252 GPa on the X-cut surface, which are different from the corresponding elastic properties of the quartz (103 GPa for the Z-cut surface and 79 GPa for the X-cut surface) [16]. The Young's modulus values of 331 GPa on Z-cut surface, or 252 GPa on X-cut surface are much higher than that of the Young's modulus for Eglin sand grains (with an average value of 90.4 GPa for assorted sand grains). These results indicate that the individual Eglin sand grains are not single crystals, rather, they are polycrystalline with polycrystalline grain sizes much smaller than the indent size so that nanoindentation will give the effective properties of an ensemble of polycrystalline grains. The effective behavior of an ensemble of polycrystalline grains is isotropic so that the Oliver and Pharr approach can be applied to determine the Young's modulus of individual sand grains.

## 2.5 Conclusions

In order to assess the granular level mechanical behavior of sand, nanoindentation was conducted on individual sand grains to characterize their mechanical properties, namely, Young's modulus, 0.2% offset yield strength, hardness, stress-strain relationship and fracture toughness. Mechanical proper-

ties of six sizes of sand grains, namely 0.600 mm, 0.500 mm, 0.425 mm, 0.300 mm, 0.212 mm and 0.150 mm, were measured to investigate the particle size effect. The properties of sand at granular level have a wide variation, and follow the Weibull distribution. Larger sand grains were found in general to have higher Young's modulus and hardness. The overall Young's modulus for the Eglin sand grains was found to be around 90.4 GPa (range 33.4 to 119.8 GPa), hardness to be 12.8 GPa (range 4.2 to 20.3 GPa and fracture toughness to be 2.32 MPa.m<sup>0.5</sup> (range 1.3 to 4.0 MPa.m<sup>0.5</sup>). The maximum Young's modulus, hardness were attained at the median grain size of 0.425 mm, indicating that the nature has optimized the sand grain size by selecting the median sand grains to have the highest mechanical properties. Ramberg-Osgood power-law relationship was used to describe the homogeneous and isotropic stress-strain behavior for sand at the granular level through FEM simulation of the nanoindentation, and the material parameters was determined. These data can be used for mesoscale simulations of sand with the Weibull distributions through such methods as the stochastic mechanics in the future.

## Chapter 3

# Static Compression of Sand

*This study was conducted by Vijay Subramanian at Oklahoma State University. The details of this study are documented as MS thesis [52] and a journal article is currently under preparation for submission to the Experimental Mechanics journal.*

Mechanical behavior of sand has been of interest to civil and military engineering. Unlike metals, which have been extensively studied and their behavior successfully modeled in view of their continuum nature, mechanical behavior of granular materials still remain a challenge [2, 3, 9, 31]. Bulk modeling based on continuum assumption of granular materials requires consideration of additional factors, such as particle size distribution, grain-grain contact, fracture of particles, friction between the particles. They are complicated by the heterogeneity in shape and particle sizes. Extensive experimental characterization of the sand behavior under different loading conditions would be required to develop meaningful constitutive models. The current lack of such constitutive laws for granular materials shows the complexity of modeling the static as well as dynamic behavior of sand. Various factors have been identified that influence the behavior of sand, including initial packing density, particle size and their distribution, as well as the shape of the grains, strength of individual grains, moisture content, confinement pressures, loading rate, etc.

Sand in the mine shafts and earthen dams experience pressures of  $\sim 7$  MPa whereas deep well shafts experience pressures nearly ten times the value

(up to 70 MPa) [62]. Pile foundations exert pressures of 350 MPa in the soil under the tips of the pile drivers [41]. Models developed thus far to describe the compressive behavior of sand are for low pressures and have been validated at pressures below 100 MPa. Sand has been observed to undergo higher stresses in the case of projectile penetrating in sand [2, 3], explosion sites [30], and even packing of spent nuclear fuels in pressurized containers [23].

Terzaghi and Peck [55] conducted compression experiments on sand up to 96 MPa and observed particle crushing. Allen *et al.* [2, 3] conducted projectile penetration experiments on sand confined in a box. They observed extensive grain crushing along the trail of the projectile. Static experiments were conducted to investigate the extent of grain crushing as a function of axial stress. Sand was confined in a steel cylinder and compressed to a maximum axial stress of 600 MPa. They noted the onset of grain crushing to occur at  $\sim 10$  MPa which was considered to be the threshold value for comminution of sand grains.

Hendron [29] reported a series of uniaxial compression experiments aimed at investigating the effect of initial density of various sands on the stress-strain behavior. Dense sand produced a steeper stress-strain curve compared to loosely packed sand sample. The stress levels at which sand crushing occurred increased as the initial density increased. This is related to the ability of loose sand to rearrange to a greater extent thus preventing the early onset of cracking. The average stress levels at which fracture of sand grains occurs was found to be significantly higher with increasing initial density. The energy absorption in uniaxial compression of sand at high pressures was understood to include the following factors: (a) the rearrangement of grains leading to permanent reduction in actual volume, (b) the crushing of the grains leading to the creation of new surfaces, and (c) friction due to relative sliding of the grains causing elastic hysteresis in strains. Hendron postulated that a large extent of crushing in bigger sand grains to occur due to increased inter-particle stresses which vary inversely with the particle size.

Vesic and Clough [57] reported the results of a series of triaxial tests in which the maximum confinement pressures reached 69 MPa (10,000 psi), which they considered as ‘high pressures’. They cited the need for triaxial testing of sands at pressures exceeding 6.9 MPa (1,000 psi) to predict soil behavior in deep wells, tunnels, and nuclear blast sites. They also reported that dense sand behaved differently at higher pressures than at lower pressures. Below 1 MPa, they observed very little crushing and the dilatation was pronounced, due to the ability of sand grains to rearrange. Crushing of grains intensified between 1 MPa and 10 MPa.

Hagerty *et al.* [25] conducted uniaxial compression tests on sand at a maximum axial pressure of 689 MPa. They conducted experiments at high pressures to investigate the effect of initial packing density, angularity of particles, and particle mineralogy. They showed that spherical Ottawa sand exhibit less particle crushing than the angular Black Beauty sand and glass beads. The softer Ottawa sand showed greater tendency to fracture than the glass beads. Plots of the void ratio vs axial stress showed the presence of negative void ratio values at higher stresses, which was attributed to compression of the mineral particles. To circumvent the issue of negative void ratios, they presented the results in terms of axial stresses vs axial strains. The onset of crushing was detected from the change of initial loading slope in the axial stress- strain curve. This onset of crushing was called the ‘crushing stress’, denoted by  $p_c$  and the slope was called the initial moduli, denoted by  $M_i$ . Based on these experiments, a generalized stress-strain behavior of sand was proposed. The initial phase (Phase I) was denoted by the onset of particle crushing. Phase II comprised of particle crushing and particle redistribution. Further crushing occurred as the stresses are increased. This phase showed a drastic drop in the slope with increasing stress. The third phase, marked by a rapid rise in the slope, occurred as the particle rearrangement and crushing terminated with reduction in the void ratio. Crushing decreased and approached a “pseudoelastic” phase. They concluded that the particles showed significant crushing above axial stresses of  $\sim 138$  MPa, which was the limit of previous uniaxial and triaxial studies. The final moduli of dissimilar sands with

different grain sizes, shapes, and mineralogy were found to approach similar values at higher pressures.

Yamamuro *et al.* [62] performed uniaxial tests on sand attaining axial stresses of up to 850 MPa. Three different types of sands, namely, quartz, Cambria, and gypsum were chosen for their varying mineral hardness values. Of the three, quartz sand is the hardest and gypsum sand the softest. Cambria sand consisted of particles with hardness ranging between quartz at one end to gypsum at the other. Sand specimens with higher initial density attained the maximum axial stress at smaller axial strains as compared to the less dense specimen. The high stress portions of the curves appeared identical. The softer gypsum sand exhibited larger axial strains when compared to the harder quartz sand. Hardness of the sand particles influenced the stress-strain behavior, wherein the harder grains failed by brittle fracture whereas the softer grains exhibited plastic behavior. In the case of Cambria sand, the soft grains were observed to deform plastically around the harder ones. The void ratios of softer grains experienced highest reduction, almost close to zero. In all the sand types tested, the effect of initial density on the reduction of void ratio with increasing stress diminished as the void ratio curves merged. For harder quartz sand, the void ratio curves merged at higher axial stresses. The presence of moisture contributed to higher radial stresses arising from increased pressures in pores trapped with water. Experiments were conducted on sand with moisture and the effect of moisture on the stress-strain behavior was found to be negligible at higher stresses.

Martin *et al.* [40] conducted both static and dynamic tests to investigate the effect of moisture on the mechanical properties of sand. The static experiments were conducted on a uniaxial strain apparatus. Partially saturated sand exhibited less stiffness compared to dry sand in the axial stress-strain experiments. Dynamic tests on split Hopkinson pressure bar (SHPB) showed a similar trend of decreasing stiffness with increase in the moisture content. The softening of grain behavior in sand is attributed to the reduction in friction, possibly caused by the lubricating effect of water between the

grains of sand.

Recent work reported by the authors (see Luo *et al.* [37] for details) on dynamic compression of dry Eglin sand in the SHPB apparatus, showed the influence of initial mass density on the mechanical properties of sand. The initial stress-strain response of dry Eglin sand was found to be proportional to the exponent of initial mass density ratio  $(\rho_1/\rho_2)^n$ , where the exponent  $n$  was determined to be 8.25.

The current investigation is focused on the effects of initial packing density, grain size, and moisture content at low strain-rates ( $<10^{-3} \text{ s}^{-1}$ ) on the compressive behavior of passively confined sand under axial pressures of up to 3 GPa.

### 3.1 Method of Confined Compression

Ma and Ravi-Chandar [39] developed a method for characterizing the multi-axial stress-strain behavior of materials under confinement using uniaxial compression. Figure 3.2 shows a schematic of the confined compression apparatus after Ma and Ravi-Chandar. Similar apparatus was designed and built in the present investigation. The material to be tested is mounted in a hollow metallic cylinder called the confinement and axially compressed after closing the top and bottom of the cylinder with end caps, made from cemented tungsten carbide. The metallic cylinder provides the confining pressure to the sample. The presence of the confining cylinder also prevents inhomogeneous deformation in the sample, thereby relieving concerns of buckling, bulging, and shear banding. The axial stresses ( $\sigma_{zz}$ ) are measured using a load cell mounted on the test frame and axial strains ( $\epsilon_{zz}$ ) using an extensometer. The elastic response of the cylinder to the radial expansion of the sample is measured by a strain gage mounted on the outer surface of the confinement. This strain gage measures the hoop strain on the outer surface of the confinement. The measured hoop strain ( $\epsilon_h$ ) is used to determine the radial pressure acting on the sample using the Lamé solution for plane stress,

as the cylinder is free to expand axially as indicated by Eqn. (3.1).

$$\sigma_{rr} = \sigma_{\theta\theta} = \frac{(b/a)^2 - 1}{2} E_c \epsilon_h \quad (3.1)$$

where  $E_c$  is the modulus of the confinement and  $\epsilon_h$  is the measured hoop strain.

The test specimen in the confined compression apparatus is cylindrical with an outer diameter of ‘2b’ and inner diameter of ‘2a’. The specimen is carefully machined to prevent any loss of contact between the inner surface of the confinement with the outer surface of the sample. Very small tolerance is needed so that the expansion of the sample and the confinement is continuous from the start of the test. The confinement is designed such that it remains elastic throughout the test and exhibits compliance that is measurable by the hoop strain gage. The elastic condition of the confinement is to prevent the complexity in stress analysis stemming from the plastic deformation of the sleeve. Hanina *et al.* [27] and Rittel *et al.* [48] demonstrated the use of confinement beyond the elastic limit to maintain constant confinement pressure. By varying the thickness of the confinement, different confining pressures were obtained.

The state of stress and strain are obtained from the theory of elasticity [56] of the confined specimen in the cylindrical coordinate system using Eqn. (3.2). The equations are valid for confinement within the elastic range and contact between the confinement and the test specimen is assumed to be frictionless [39, 47].  $E_c$  and  $\nu_c$  are the Young’s modulus and Poisson’s ratio of the confinement. Thus, the three measured quantities provide a complete description of the stress and strain components of the material under evaluation.

$$\sigma_{rr} = \sigma_{\theta\theta} = \frac{(b/a)^2 - 1}{2} E_c \epsilon_h \quad (3.2)$$

$$\sigma_{zz} = \sigma_a \quad (3.3)$$

$$\epsilon_{rr} = \epsilon_{\theta\theta} = \frac{\epsilon_h}{2} \left[ (1 - \nu_c) + (1 + \nu_c) \frac{b^2}{a^2} \right] \quad (3.4)$$

$$\epsilon_{zz} = \epsilon_a \quad (3.5)$$

The principle stress and strain components from Eqn. (3.2) are used to derive the dilatational and shear components. The hydrostatic stress and strain components are given in Eqns. (3.6) and (3.7).

$$\text{Mean stress, } \sigma_m = \frac{\sigma_{zz} + 2\sigma_{rr}}{3} \quad (3.6)$$

$$\text{Volume dilatation, } v = \epsilon_{zz} + 2\epsilon_{rr} \quad (3.7)$$

The maximum shear stress and shear strain are given by Eqns. (3.8) and (3.9)

$$\tau_e = \frac{1}{2}(\sigma_{zz} - \sigma_{rr}) \quad (3.8)$$

$$\gamma_e = (\epsilon_{zz} - \epsilon_{rr}) \quad (3.9)$$

The three elastic constants, namely, Young's modulus, Poisson's ratio, and bulk modulus of aluminum sample were determined from a single test using the method of confined compression. This technique has also been successfully applied to characterize polymers [47], ceramics [15], borosilicate glass [14] and concrete [21].

## 3.2 Experimental Procedure

A self-aligning compression fixture was designed and fabricated to conduct high pressure compression tests on sand. As shown in Figure 3.3, the fixture assembly consists of a top steel platen, hollow steel enclosure, a steel ball, steel confinement, and two cemented tungsten carbide end caps for the cylindrical container. The fixture was designed to reach high axial stresses of up to 3 GPa in the sand sample and to overcome any misalignment in the fixture during compression. The confinement was made from hardened AISI A2 steel with an inner diameter of 6.35 mm (0.25 in.), outer diameter of 12.70 mm (0.50 in.), and length of 25.40 mm (1.00 in.). The inner bore was honed after heat treatment to reduce friction between the sample

and the confinement. Cemented tungsten carbide (WC) rods with 10 % cobalt content (binder) and submicron grain size (from Centennial Carbide) were used as the loading pins. The WC rods are 6.34 mm (0.2495 in.) in diameter and 31.75 mm (1.25 in.) long. The mechanical properties of cemented WC rods are hardness HRA 92, modulus of elasticity: 580 GPa, and compressive strength: 5.5 GPa. High strength and toughness, good surface finish and high hardness make cemented WC an ideal choice of material for compression of sand to high pressures. The rods exhibited resistance to indentation and wear by the sand grains even after several experiments. Experiments were carried out on an MTS servo-hydraulic uniaxial testing machine equipped with a 245 kN (55,078 lbf) MTS load cell and Instron Fastrack 8800D controller.

A Vishay bonded strain gage (WK-13-125BZ-10C) was mounted on the outer surface of the confinement to measure the hoop strains of the confinement as a result of lateral expansion of sand during compression. The leads from the Wheatstone bridge were connected to Vishay 2310A signal conditioner and amplifier. Experiments were performed at room temperature of 22°C. A Nicolet Sigma-30 oscilloscope (12-bit resolution) was used to acquire the analog output (0-10 V) from the signal conditioner at a sampling rate of 50 Hz. Signals from the Instron controller and Nicolet oscilloscope were synchronized. The experimental and design details are described elsewhere [52].

A  $0.4 \pm 0.0004$  grams of sand was weighed using a micro-balance (Denver Instruments APX-200 with 0.1 mg resolution) and poured into the confinement with the bottom WC end cap in place. Care was taken to prevent loss of sand grains during transfer. The top WC rod was inserted into the confinement and the assembly was compacted. Since no standardized method for compaction exist, the assembly was gripped firmly in hand and gently tapped periodically on a rubber pad. The assembly was rotated after every few taps to prevent settling of smaller sand grains. This was done to maintain the heterogeneous distribution of sand grains. The length of the assembly was measured from time to time to check if the sand specimen

was compacted to the desired packing density.

Experiments were conducted under displacement control. The bottom fixture was gradually raised till a pre-load of 40 N was reached. A displacement rate of  $2 \times 10^{-3}$  mm/s was selected which corresponds to a strain rate of  $2 \times 10^{-3} \text{ s}^{-1}$ . This value falls in the quasi-static test regime. Upon completion of the test, the crushed sand in the confinement is collected. The bore of the confinement is cleaned with 91% isopropyl alcohol using cotton tipped applicator. The confinements were re-used for different experiments until the indentation marks of the sand on the bore of the confinement were prevalently seen. Yielding in the confinement was not observed as the output of the hoop strain gage showed repeatability in the sample experiments done at the highest density of sand ( $1.70 \text{ g/cm}^3$ ) that was tested. Care was taken to ensure that the sample was placed in the mid-length of the confinement to ensure accurate measurement of the hoop stresses by the strain gage mounted on the confinement. At least three experiments were conducted under each testing condition to examine the repeatability of the measurements.

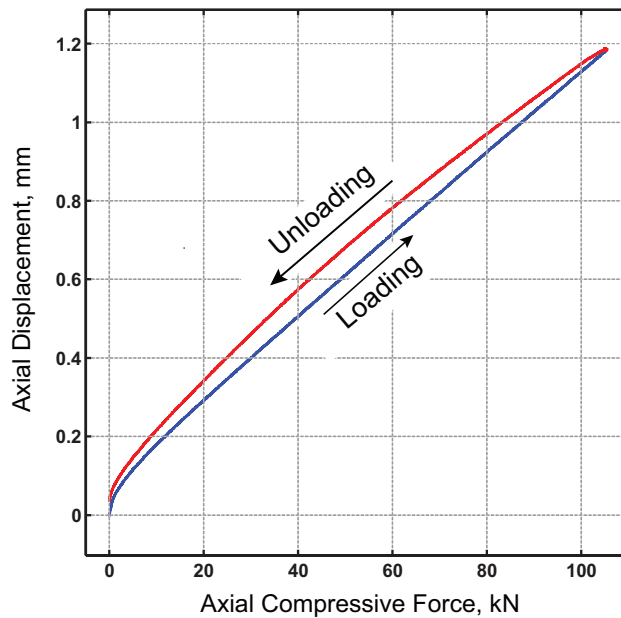


Figure 3.1: Load-displacement plot showing the compliance of the system without the sand sample.

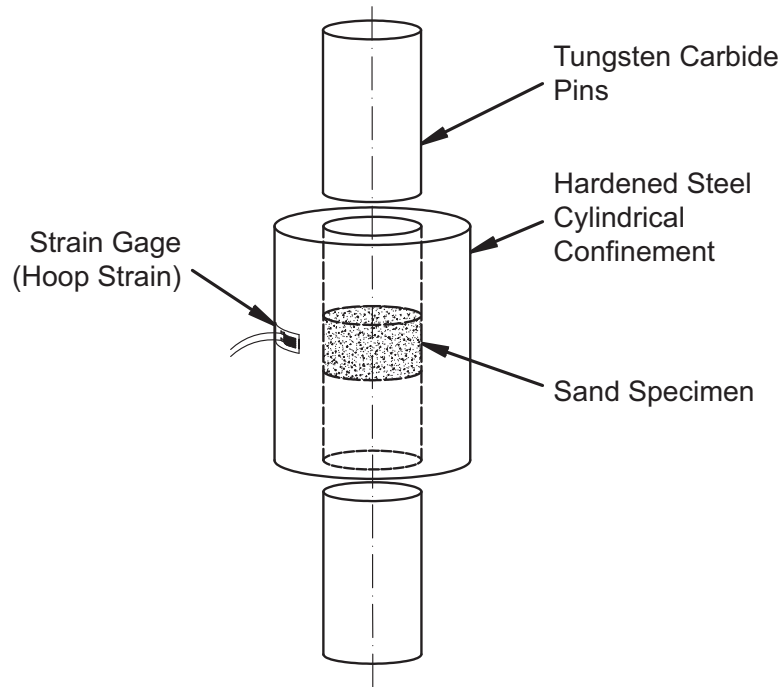


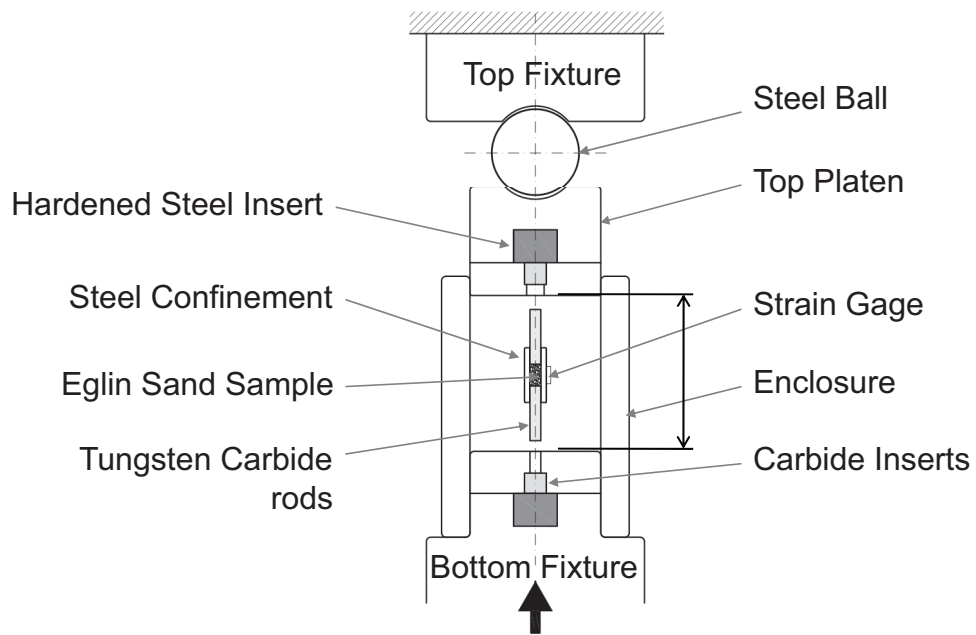
Figure 3.2: Schematic of self-aligning static compression fixture

### 3.3 Results and Discussion

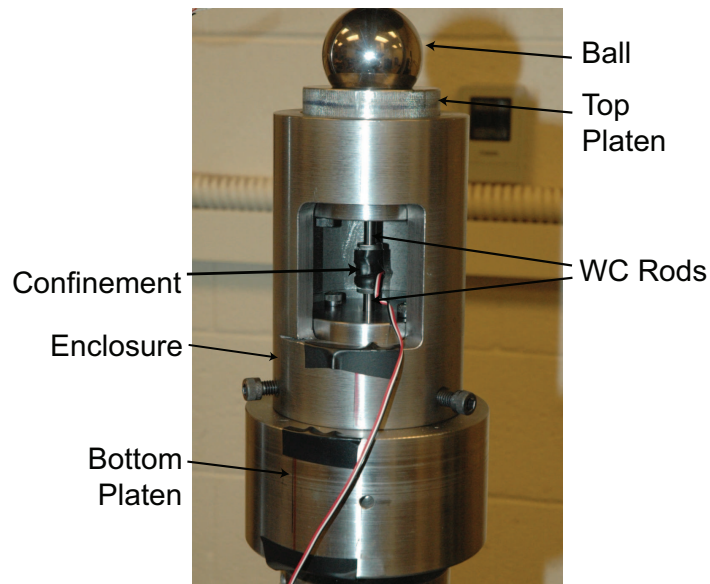
The results of tests conducted on Eglin sand are documented elsewhere [52]. In this section the effects of initial mass density, particle size, and moisture content on the multi-axial mechanical behavior of sand are described.

#### Effect of System Compliance

To accurately determine the specimen strains, it is necessary to determine the compliance of the load frame (including the fixture) for no system is infinitely rigid and the force (100 kN) involved was sufficient to induce displacement in the machine. Compliance in the system arises from the deflection of individual components in the load frame which can be significant at high loads. The compliance tests were performed up to a maximum load of 103 kN. Figure 3.1 shows the deflection in the system during loading and unloading of the WC end caps without the sand sample. The load-displacement curve shows an initial bend after which the loading curve remains linear. The unloading curve exhibits some hysteresis with a non-linear response. Tests performed on the load frame without the fixture in



(a)



(b)

Figure 3.3: Schematic (a) and photograph (b) of the self-aligning static compression fixture.

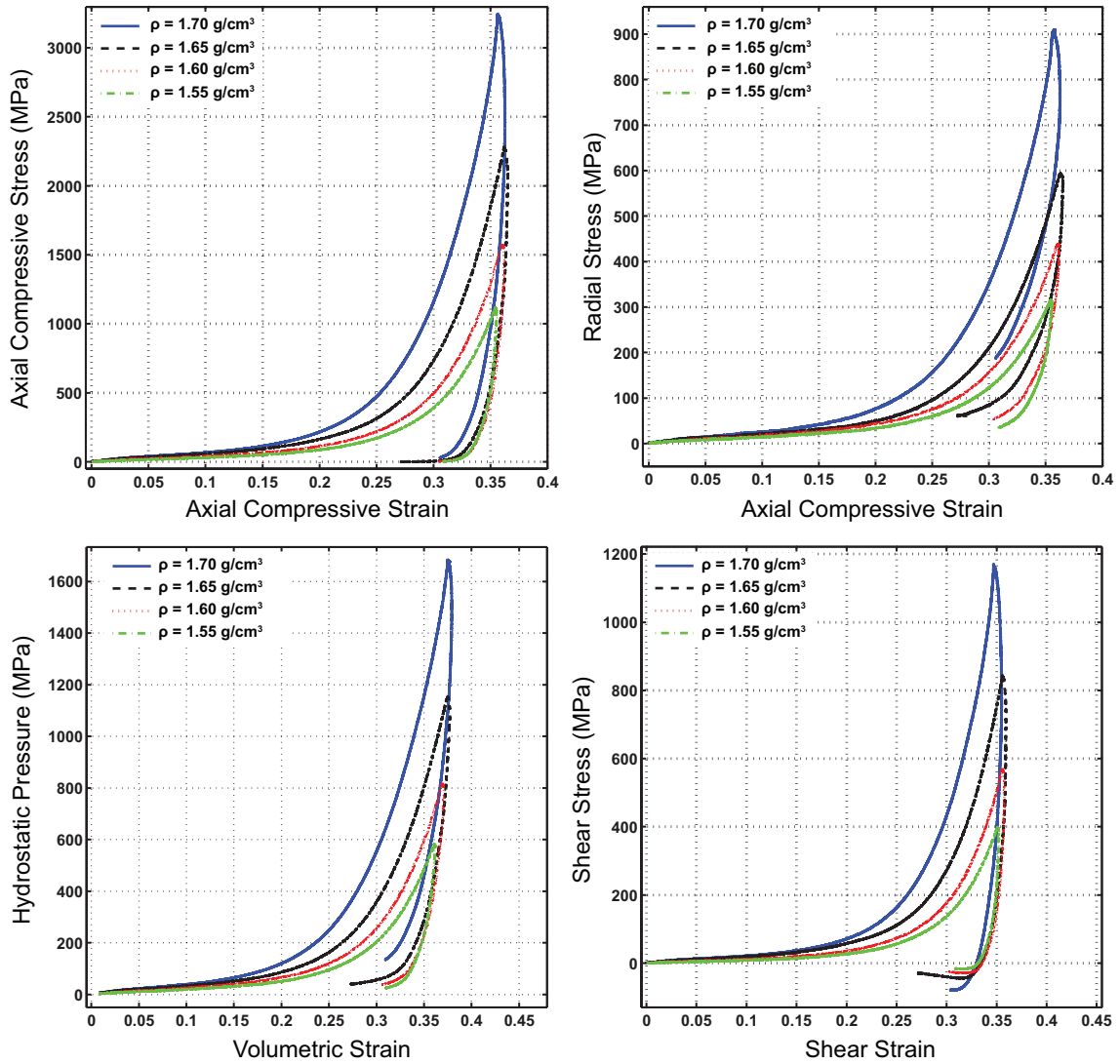


Figure 3.4: Linear plots of stress vs. strain for sand densities of 1.55, 1.60, 1.65, and 1.70  $\text{g/cm}^3$  showing increase in stiffness with increase in initial density.

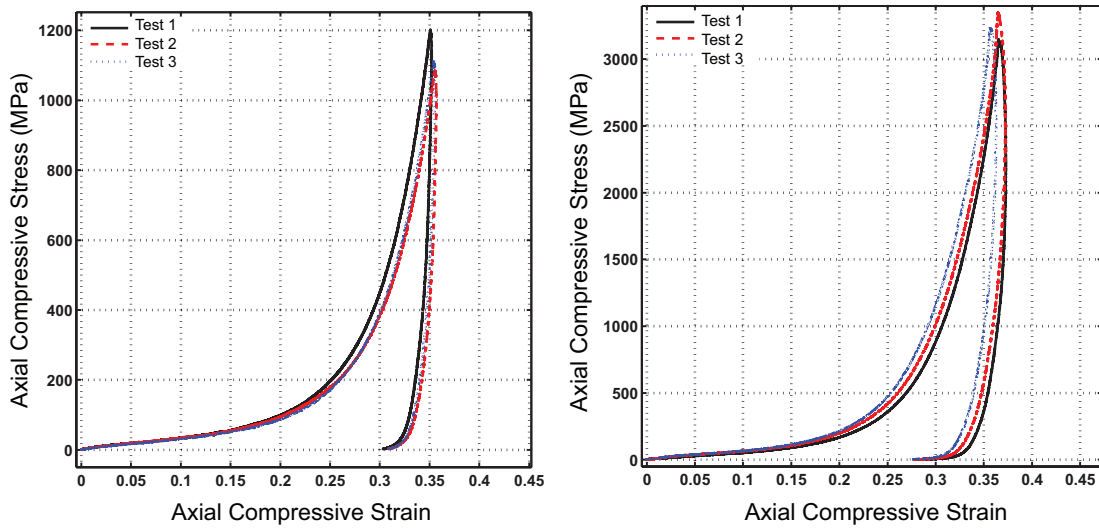


Figure 3.5: Linear plots of axial stress vs. axial strain conducted at low ( $1.55 \text{ g/cm}^3$ ) and high ( $1.70 \text{ g/cm}^3$ ) initial densities, showing experimental repeatability.

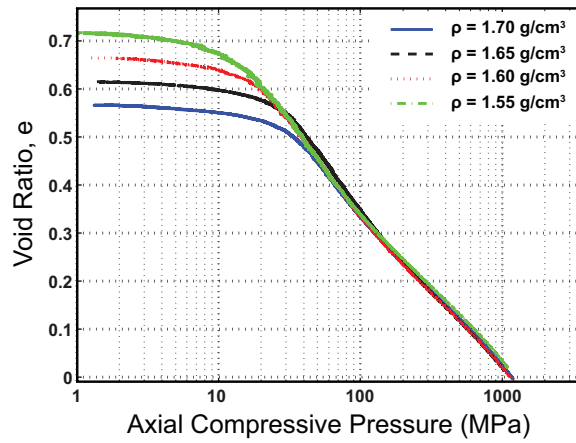


Figure 3.6: Semi-log plot of void ratio vs. axial stress for sand densities of  $1.55$ ,  $1.60$ ,  $1.65$ , and  $1.70 \text{ g/cm}^3$  showing unification of curves below  $e = 0.5$ . The void ratio curves approach zero beyond  $1 \text{ GPa}$  axial pressures.

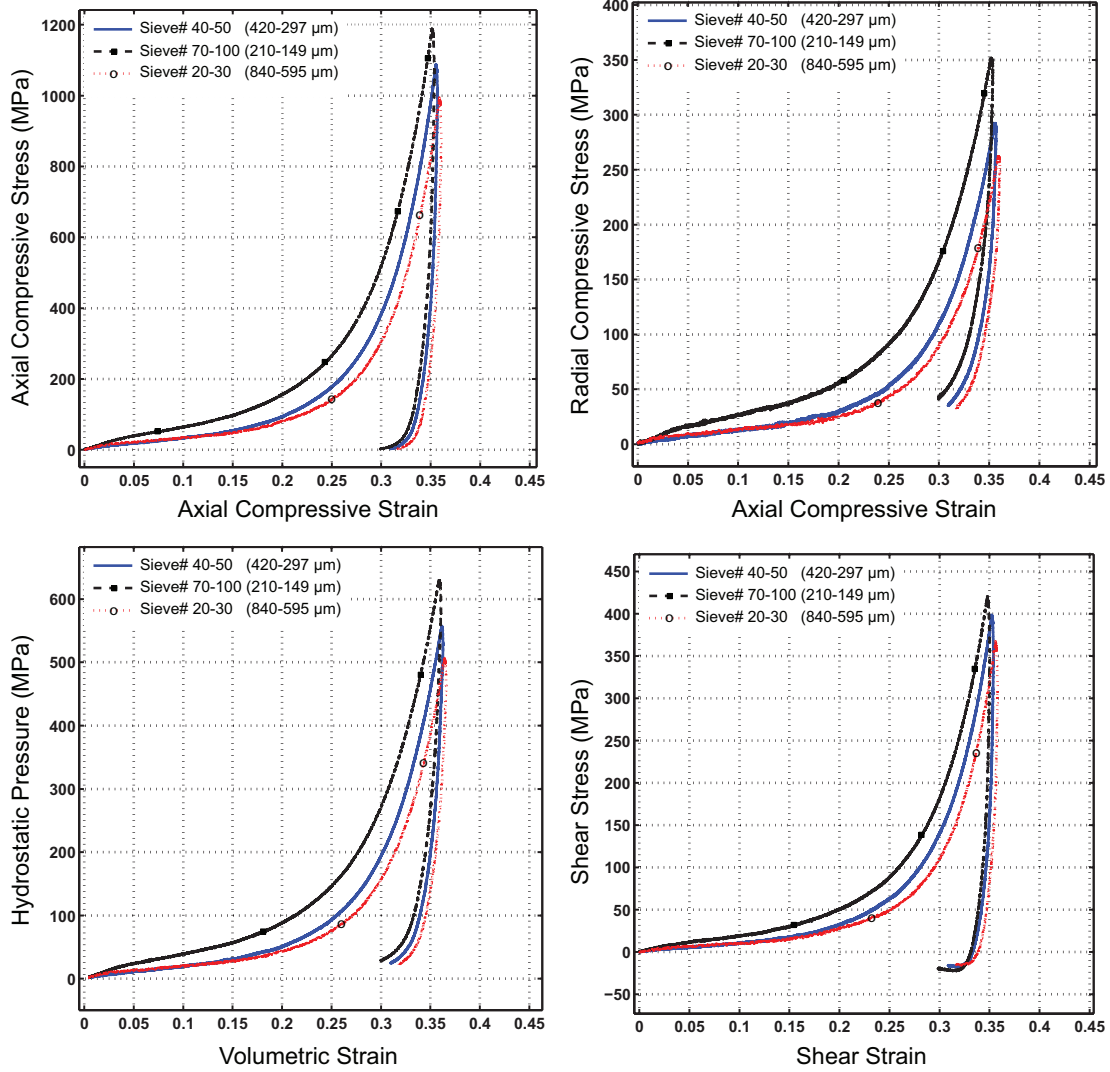


Figure 3.7: Linear plots of stress vs. strain for sand sieve sizes of 100 (fine), 30 (coarse), and Eglin sand at initial density of  $1.55 \text{ g/cm}^3$ .

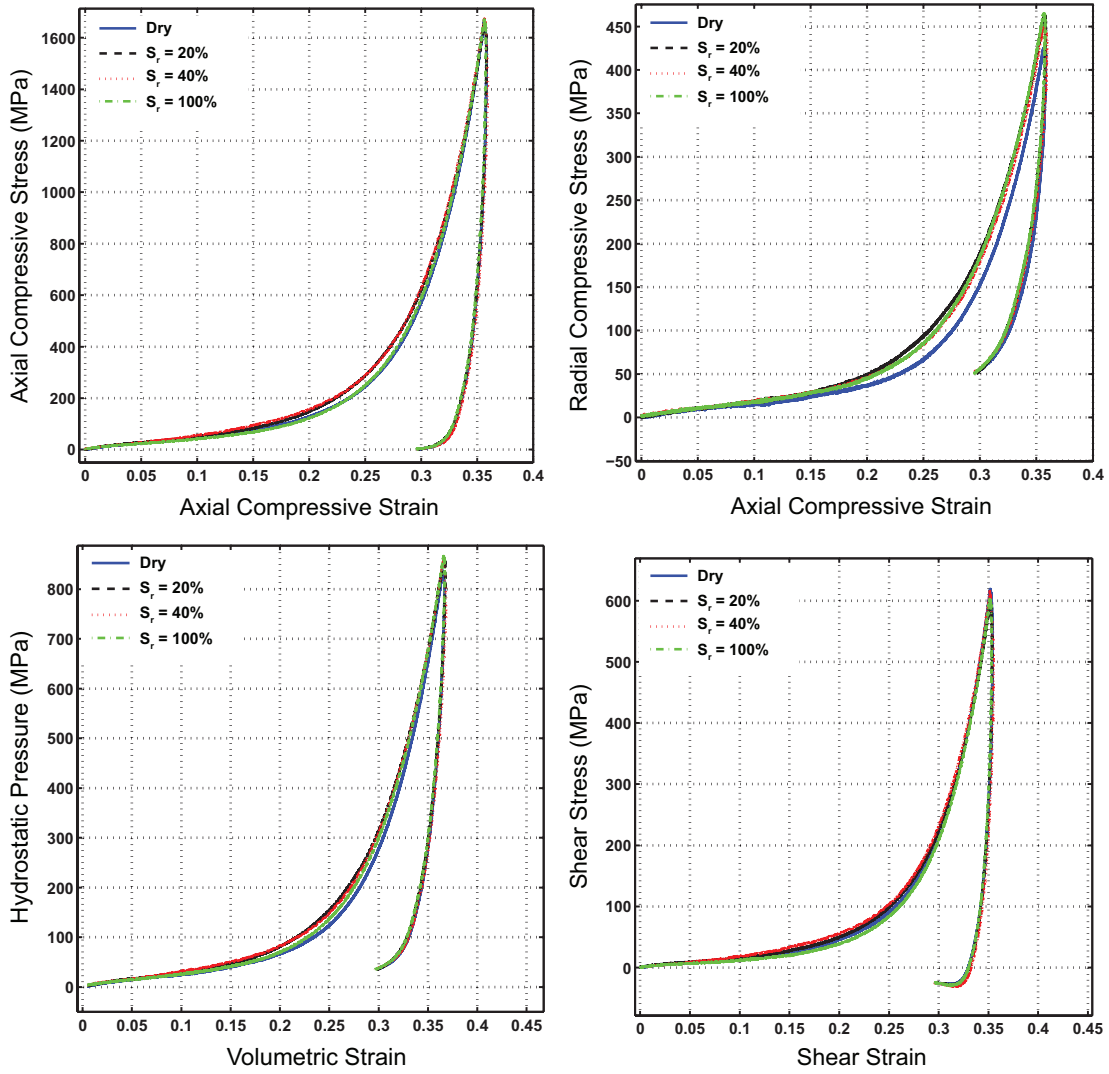


Figure 3.8: Linear plots of stress vs. strain for 0%, 20%, 40%, and 100% water saturation in the sand samples.

place show the presence of hysteresis in the load-deflection data, thereby showing that the cause of the hysteresis is in the load frame rather than in the fixture or the sand sample. A 10<sup>th</sup> order polynomial curve was fitted on the loading and unloading curves to obtain continuous polynomial functions for the loading and unloading cycles. Ideally the loading and unloading curves of tests on sand sample can be corrected for compliance using the curve fits obtained from the compliance tests. Due to the difficulty in implementing individual corrections, the loading compliance curve was used for compliance correction of both loading and unloading paths in the tests conducted on sand.

### **Effect of Initial Density**

Results of experiments conducted to investigate the effect of initial density of dry sand on its mechanical behavior are shown in Figure 3.4. The minimum density of 1.55 g/cm<sup>3</sup> was attained by pouring sand into the confinement and gently tapping it a few times to reach a sample length of 8.21 mm. Maximum density of 1.70 g/cm<sup>3</sup> was attained by gently tapping the assembly for an extended period of time to reach a length of 7.49 mm. Three experiments were conducted at each packing density for repeatability. Figures 3.5(a) and 3.5(b) show the repeatability in the axial stress-strain behavior for the lowest and highest initial densities. All experiments were conducted up to a maximum axial compressive strain of 35% after compliance correction. Axial strain of 35% (after compliance correction) was chosen based on the limitations of the test frame and the compression fixture. Experiments conducted on the most dense configuration of sand, namely, 1.70 g/cm<sup>3</sup> reached a maximum axial stress of 3.2 GPa at corresponding axial strain of 35%.

Four Eglin sand samples with nominal densities, namely, 1.55, 1.60, 1.65, and 1.70 g/cm<sup>3</sup> were compressed to 35% axial strain at 0.002 s<sup>-1</sup> strain rate. Figure 3.4 shows the axial stress vs. axial strain and radial stress vs. axial strain from the measured axial load, axial displacement, and circumferential displacement. The derived quantities, namely, hydrostatic

stress vs. volumetric strain and the shear stress vs. shear strain are also shown in Figure 3.4.

The linear plot of axial stress-axial strain curves in Figure 3.4(a) exhibit two linear trends in the loading region followed by an unloading curve. The first linear region is observed while loading from rest, up to an axial strain of 2.5 %. The second linear region is observed between 30 % and 35 % axial strains. The initial loading curve transitions to a steep ascent from  $\sim 10$  % axial strain.

The plots shown in Figure 3.4 follow the general three phase behavior proposed by Hagerty *et al.* [25]. The first linear trend is observed to occur in the initial portion of the loading curve between 0% to 0.5% axial strain. They defined the slope of the initial portion of the loading curve as the initial modulus ( $M_i$ ). The initial linear slope for the four densities investigated are found to be the same,  $M_i = 10$  MPa. This is likely to be due to the elastic compression of the sand grains during the initial loading phase. The initial linear region is terminated at  $\sim 2.5$  % which corresponds to an axial stress below 50 MPa, after which particle crushing begins. This region is marked by a sharp drop in the slope of the stress-strain curve. The axial stress-axial strain plot shows the dependence of the onset of particle crushing on the initial density. The break-point stress is found to increase with increase in initial density. This is found to be in general agreement with the results of Hagerty *et al.* [25] and Hendron [29]. The break-point stress becomes less distinguishable as the initial density increases. In the semi-log curve of axial stress versus axial strain, as shown in Figure 3.4(a), the break-point stresses for 1.70 and 1.65 g/cm<sup>3</sup> are very similar, whereas for samples at densities of 1.55, 1.60, and 1.65 g/cm<sup>3</sup> exhibit clear onset of particle crushing.

Crushing and reorganization of sand particles are found to be gradual in loosely packed sand than in dense sand. The higher packing densities of densely packed sand constrain the rearrangement of the sand grains which lead to the build-up of higher stresses. Thus the duration of grain crushing in densely packed sand is shorter than that of loosely packed sands. The

Table 3.1: Mechanical properties of Eglin sand at different initial densities.

Initial Density $\rho$ (g/cm <sup>3</sup> )	Final Constrained Modulus			Max. Axial Stress $\sigma_{zz}$ (GPa)	Max. Radial Stress $\sigma_{rr}$ (GPa)
	Young's Modulus E (GPa)	Bulk Modulus K (GPa)	Shear Modulus G (GPa)		
1.70	104	27.9	30.7	3.24	0.91
1.65	40	23.3	18.3	2.23	0.59
1.60	29	11.9	11.5	1.66	0.42
1.55	20	8.6	7.4	0.95	0.31

transitional phase of grain crushing is gradually followed by the pseudo elastic compression phase, where the crushed grains behave much stiffer than in the initial uncrushed phase. Hagerty *et al.* [25] defined the slope of the final pseudo elastic phase as the final constrained modulus ( $M_f$ ). During the final pseudo elastic phase, the voids are filled with fine comminuted particles and show much higher stiffness. Hence,  $M_f$  is found to be much higher than  $M_i$ . Similar trends are observed in the radial, hydrostatic, and shear stress-shear strain curves. The values of the slopes obtained from the various stress-strain curves are called the apparent modulus, as they represent the slope of the bulk rather than the individual grains of sand. Various values of apparent moduli are given in Table 3.1. The elastic modulus of sand, obtained from nanoindentation experiments conducted on single sand grains by Daphalapurkar *et al.* [17], is  $\sim 90$  GPa, with values ranging from 70 to 110 GPa. This closely matches with the value of apparent E obtained at  $\rho = 1.70$  g/cm<sup>3</sup>, which is 104 GPa. At  $\rho = 1.70$  g/cm<sup>3</sup>, the sand is in a highly dense state of packing with minimal voids. This prevents the sand from undergoing extensive rearrangement and rotation, thus crushing them to a powder form at stresses  $\sim 3$  GPa. The crushed sand from these experiments were sieved and found to be below 75  $\mu\text{m}$  in size. Since a small mass (0.4 g) of sand was tested, particle size distribution by sieve analysis was not conducted. The powdered sand at  $\rho = 1.70$  g/cm<sup>3</sup> showed modulus values close to that of single sand grains.

The unloading phase is marked by a rapid drop in the axial stress for small changes in the axial strain. This indicates a small elastic recovery possibly

from the pseudo elastic compression phase. A small negative slope is seen in the unloading curves for sand densities of 1.65 and 1.70 g/cm<sup>3</sup> as shown in Figure 3.4(a). This behavior can be attributed to the use of the loading compliance curve for compliance correction, although similar behavior is also observed in the radial stress-strain plots shown in Figure 3.4(b). The negative slope indicates an increase in stress during the start of unloading when the strain is reduced in the sample. It is not clear at this stage if this behavior is due to the machine compliance or from the mechanical response of crushed sand. The extent of elastic recovery is similar for all densities, indicating that the elastic strain energy accumulated in the pseudo elastic phase is recovered during unloading. However, the radial stresses show similar negative slopes during unloading.

The semi-log plot of void-ratio versus axial stress shown in Figure 3.6, is typically used in the soil mechanics community to visualize the degree of sand crushing as a function of axial stress. Densely packed sand has lesser voids than loosely packed sand. The void ratio curve is found to be in agreement with the trend observed in the void ratio curves of Yamamuro *et al.* [62]. The initial slope on a semi-log plot shows a linear phase for axial stresses below 10 MPa. This linear phase is followed by rapid collapse of voids with increase in axial stress. The void ratio curves for different densities are found to converge along a common path. Similar merging of void ratio curves has been reported by Hagerty *et al.* [25] and Yamamuro *et al.* [62]. For densely packed sand, namely, 1.70 and 1.65 g/cm<sup>3</sup>, the void ratio curves extend to the negative values at axial stresses above 1 GPa. The presence of negative void ratios is considered to be due to compression of the mineral particles, as noted by Hagerty *et al.* [25].

#### **Effect of Particle Size**

To investigate the effect of particle size on the mechanical behavior of sand three particle sizes were chosen: (i) passing sieve #20 but stopped by sieve #30 (20-30), (ii) passing sieve #40 but stopped by sieve#50 (40-50) and (iii) passing sieve #70 but stopped by sieve #100 (70-100). All exper-

iments were conducted at an initial density of  $1.55 \text{ g/cm}^3$ . Figure 3.7(a) shows the axial stress versus axial strain responses of sand particles. The smaller particles of sieve size 70-100 showed a stiffer response as compared to larger particles of sieve size 20-30. The radial stress versus axial strain plots, shown in Figure 3.7(b), exhibit a similar trend, namely, increasing slope with decrease in particle size.

#### **Effect of Moisture Content**

The role of moisture on the mechanical behavior of sand was investigated at four different levels of saturation of water, namely, 0% (dry), 20%, 40%, and 100% (fully saturated) at the initial density of  $1.60 \text{ g/cm}^3$ . Figure 3.8 show the plots of axial, radial, hydrostatic, and shear stress-strain behavior. It can be seen that under quasi-static loading conditions, moisture does not seem to influence the stress-strain behavior of sand under high pressures (axial pressures up to 1.6 GPa in this investigation) . These results are in agreement with those reported by Yamamuro *et al.* [62] at 850 MPa in axial compressive pressure. Consequently, the mechanical properties namely, Young's modulus, Bulk modulus, and shear modulus of sand derived from the axial, hydrostatic, and shear stress-strain plots, also exhibit no influence of moisture content.

The presence of friction between the sand particles and the inner walls of the confinement is a source of concern. Previous investigations by many researchers acknowledged this issue. Yamamuro *et al.* [62] attempted to reduce friction between sand and the confining walls by lubricating the interface. This lead to alteration in the response of sand. Martin *et al.* [40] noted the difficulty in measuring the sidewall friction. In this investigation, sidewall friction was minimized by reducing the sample length and honing the inner surface of the confinement. The overlapping curves of the experiments conducted with different saturations of water also indicated the effect of sidewall friction to be negligible.

### 3.4 Conclusions

Quasistatic experiments were conducted on dry (Eglin) sand using a steel confinement and a self-aligning compression fixture up to axial strains of  $\sim 35\%$ . A maximum axial stress of 3 GPa was attained in the dense sand samples of  $\rho = 1.70 \text{ g/cm}^3$ . Four densities of sand, namely,  $\rho$  of 1.55, 1.60, 1.65, and  $1.70 \text{ g/cm}^3$  were tested. The radial pressure acting on the confined sand was obtained from the circumferential strain measured using a strain gage mounted on the steel confinement. The radial pressures and axial stresses as functions of axial strain were obtained. The hydrostatic and shear behavior were derived from the experimental values of stresses and strains. The values of the apparent moduli were obtained. The mean and shear behavior show significant dependence on the effect of initial density. At the highest density tested, namely,  $\rho = 1.70 \text{ g/cm}^3$ , the value of apparent elastic modulus matched closely with the values of Young's modulus ( $E$ ) obtained from single sand grains, which is  $\sim 90 \text{ GPa}$ . Crushing of sand grains commences at an axial strain of 2.5% and axial stress  $< 50 \text{ MPa}$ . The stress-strains relationships obtained can be analyzed further to facilitate the development of constitutive models for sand.

## Chapter 4

# Dynamic Compression of Sand

*This work was conducted by Huiyang Luo at Oklahoma State University. The details of this work are published elsewhere [37]*

It is well known that dense or highly compacted sand has high compressive strength and high energy absorption capacity. Sand is often used to provide ballistic protection for military structures, at the riverbeds to prevent erosion of soil, among many applications. While numerous publications exist on sand for geological and civil engineering applications, they focus on the mechanical behavior at low stress levels, on the order of tens of MPa under quasi-static loading conditions [23, 62]. Its mechanical behavior under relatively high stresses and at high strain rates is not well characterized/understood. Several difficulties are encountered in dynamic characterization of dense sand. They include the difficulty in the preparation of sand samples with consistent values of densities for use on dynamic compression using a split Hopkinson pressure bar (SHPB), the mechanical impedance change encompassing both low mechanical impedance at low compressive strain and high mechanical impedance at high compressive strain in a single experiment, resulting in difficulty to achieve dynamic stress equilibrium state on a sand specimen at low strains while achieving high stress level at higher strain levels. It is only in recent years when some relevant experimental techniques have been developed to overcome these difficulties to press on the characterization of the mechanical behavior of sand at high strain rates accurately.

Some research has been reported on sand at high strain rates, for example, the effect of saturation levels on silica sand [13], mechanical behavior of soft soil confined in a steel jacket [10], clayey, silty compacted sand [20] and dry sand [11], effect of moisture on sand properties [58] at several low compressive stress levels, as well as the mechanical behavior of dry sand under single pulse loading [49]. For dense sand under initial loading, its mechanical impedance is low. Pulse shaping techniques developed in recent years on SHPB can facilitate in establishing dynamic equilibrium and constant strain rate conditions necessary in a valid dynamic compression tests [40, 51]. For dynamic behavior of sand, a modified SHPB using a pulse shaping technique has been used to characterize the behavior of sand confined in a steel sleeve to determine the effects of moisture [40], strain rate, and confinement [51] up to a stress level of 100 MPa. In dynamic compression, as the sand sample is compressed, compaction will take place inducing significantly stiffened mechanical response. Consequently, a modified SHPB has to have the capability to apply high stresses over a relatively long loading time. In this report, we present the dynamic multi-axial compression behavior of Eglin sand with effects of density, confinement, moisture, and high-speed deformation.

In this investigation, a modified long ( $\sim 15$  m) SHPB was used with pulse shaping to allow relatively long loading time ( $\sim 1.5$  ms) to reach high compressive strains [36, 38]. The SHPB consists of a solid 304L stainless steel bars (7.5 m incident and 3.66 m transmission bars) with an outer diameter of 19 mm, and a strain data acquisition system, as schematically shown in Figure 4.1. Sand comes in loose form and is normally filled in a cavity to form a sample for testing. The experimental data depends significantly on the initial density of the sample. To enable preparation of consistent sand samples, we developed an assembly that can be used to prepare consistent sand specimens and then directly use in SHPB for dynamic compression. This was accomplished by taking advantage of the mechanical impedance match of a 12.70 mm diameter cemented tungsten carbide (WC) rod and a 19 mm diameter steel bar [34, 38]. We first fill the sand grains in a 3.18 mm thick hollow steel cylinder with one end closed by

the WC rod, and then close the other end of the cylinder with another WC rod as shown in Figure 4.2. The total mass of the assembly, including sand, is less than 200 g, so that it can be easily shaken by hand or other specially designed shaking equipments later to consolidate the sand sample to reach different density levels. The net mass of the sand (2 g) was determined by weighing (Denver Instrument APX-200, 0.1 mg resolution) the overall assembly minus the tare (steel sleeve and WC rods). The length of the cavity occupied by sand was measured by the change in length of the two WC rods from the state when the two rods are in direct contact (no sand in the hollow cylinder) and when sand grains are between two rods. These values were converted to mass density of the sand sample. Depending on the time it takes to shake the assembly, sand samples with different sand densities can be easily prepared with consistency.

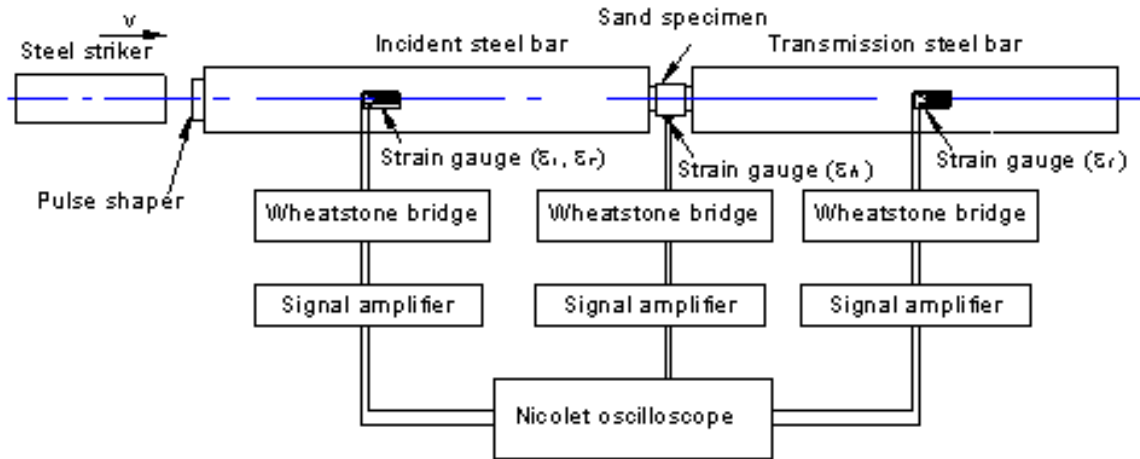


Figure 4.1: Schematic of SHPB setup for testing confined sand.

A strain gage was mounted on the external surface of the confinement steel sleeve to measure circumferential strain simultaneously with other strain signals recorded on strain gages mounted on the SHPB. This arrangement allows characterization of multi-axial compression response that can be further analyzed to determine the volumetric and deviatoric behaviors of sand. Further analysis yields other relationships, such as shear-hydrostatic

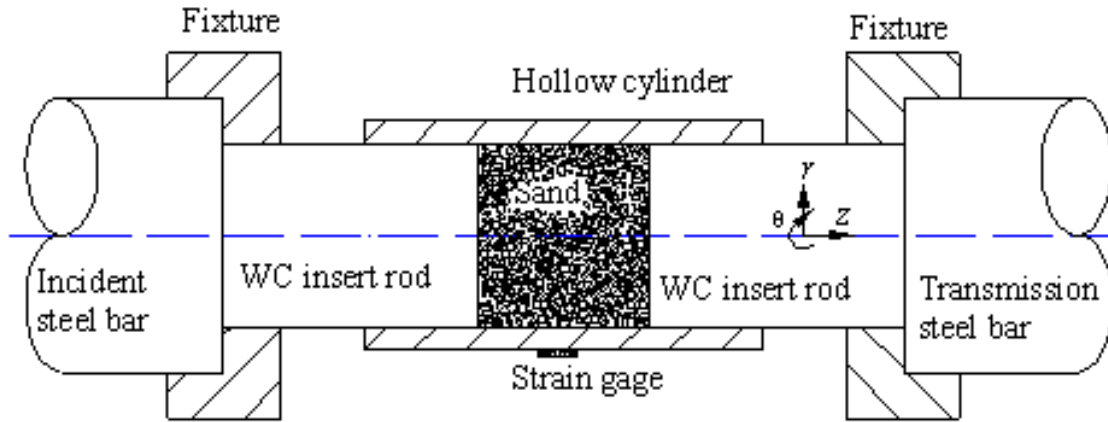


Figure 4.2: Schematic of the test section for sand assembly on SHPB setup, polar coordinates are defined as shown.

pressure behavior in the form of Mohr-Coulomb relation, the void ratio-pressure relationship to characterize sand compressibility at high strain rates. In each experiment, the sand assembly was sandwiched between incident and transmission bars. Loading was applied on the sand sample through WC rods in direct contact with the sand sample. The initial, uncompacted sand as poured and stacked together had a mass density of  $1.51 \text{ g/cm}^3$ . After shaking the assembly manually for  $\sim 10$  minutes, a density of  $1.65 \text{ g/cm}^3$  is achieved. Shaking for  $\sim 30$  minutes yields a density of  $1.75 \text{ g/cm}^3$ . In our tests, further shaking did not increase the density any further.

A copper disk of diameter 11.4 mm with thickness varying from 1.6 to 2.4 mm was used as a pulse shaper mounted on the impact surface of the incident bar in each experiment. The striker, launched by compressed air in the gas gun, impacts the pulse shaper, and generates a smooth modified compressive wave traveling in the incident bar to induce constant strain rate in the sand sample. A Nicolet Sigma-30 digital oscilloscope (12-bit resolution, 10 Ms/s sampling rate) was used to acquire strain signals through a Wheatstone bridge and a Vishay 2310A signal conditioning amplifier. Details on the experimental setup [36, 38] and the principle of SHPB [33]

have been well documented in the literature.

Under a valid experiment in which a specimen is loaded by equal stresses from both ends, the compressive stress in the specimen,  $\sigma_z$ , is calculated from transmission bar signal [34–36, 38] using  $\sigma_z(t) = (\frac{A_t}{A_s} E_0 \epsilon_t(t))$ , where  $A_s$  and  $A_t$  are the cross sectional areas of the specimen and the transmission bar, respectively;  $E_0$  is Young's modulus of the bars;  $\epsilon_t$  is the strain on the transmission bar;  $z$  is in axial direction of the sand sample, which is also the loading direction (Figure 4.2). The strain rate in the specimen is calculated using  $\dot{\epsilon}_z(t) = \frac{2c_0}{L_s} \epsilon_r(t)$ , where  $c_0$  is bar wave speed;  $L_s$  is the length of the specimen;  $\epsilon_r$  is the reflected strain wave measured on the incident bar. Integration of strain rate with respect to time gives the strain history. With known stress and strain histories, the stress-strain curves at high strain rates can be obtained. All experiments were conducted at room temperature and  $\sim 26\%$  relative humidity. For each testing condition, eight samples were tested to obtain consistent results, and the average values are reported.

For a sand sample confined by a hollow cylinder within the elastic range [24, 39], the confinement pressure (radial and circumferential) applied on the sample is calculated as  $\sigma_{rr} = \sigma_{\theta\theta} = 0.5(\alpha^2 - 1)E_c \epsilon_h$  and the hoop strain as  $\epsilon_{rr} = \epsilon_{\theta\theta} = \epsilon_h \frac{[(1-\nu_c) + (1+\nu_c)\alpha^2]}{2}$ ; where  $\alpha$  is the ratio of the outer to the inner diameters of the tubing;  $E_c$ ,  $\nu_c$  and  $\epsilon_h$  are Young's modulus, Poisson's ratio of the tubing and measured circumferential strain on tube surface, respectively;  $r$  and  $\theta$  represent the radial and circumferential directions (Figure 4.2), respectively. For the hardened steel tubing, Young's modulus and yield strength are taken as 200 GPa and 1.5 GPa, respectively. The hydrostatic pressure (isotropic stress) component  $\sigma_m$  and the volumetric dilatation  $\epsilon_m$  are given as  $\sigma_m = \frac{(\sigma_{zz} + 2\sigma_{zz})}{3}$  and  $\epsilon_m = \epsilon_{zz} + 2\epsilon_{rr}$ , respectively. The maximum shear stress  $\tau_e$  and shear strain  $\gamma_e$  are given as  $\tau_e = 0.5(\sigma_z - \sigma_r)$  and  $\gamma_e = (\epsilon_z - \epsilon_r)$ , respectively.

## 4.1 Results

### 4.1.1 Sand Specimen Assembly

The color of individual Eglin sand grains are yellow (either transparent or translucent) under an optical microscope, as observed from the end surface of a pristine sand sample after shaking. The pristine sand shows gaps between sand grains, and the small size grains are hidden underneath large sand grains. As the voids between sand grains become smaller, some smaller sand grains become visible on the surface. After SHPB impact test, most sand grains were crushed into powders with only some sand grains remaining in relatively large size. However, there are a few sand grains showing red, gray and black colors due to inclusions in the sample. The pristine sand sample shows gaps (voids) between sand grains with the small size grains sandwiched between the larger ones. Under PC, aluminum, and steel tubing confinement, the size distribution curve was almost overlapped, indicating that both aluminum and steel confinements lead to about the same size distribution after impact under confinement pressure higher than 35 MPa. Also, the crushed sand grains show uniformity in the coefficients  $U$  as 5.19, 7.30 and 6.82 for PVC, PC, and steel tubing, respectively, indicating poor uniformity. The  $d_{60}$ ,  $d_{10}$  and  $U$  values are determined as 0.225 mm, 0.033 mm and 6.82, respectively, indicating a large size variation for the crushed sand.

### 4.1.2 Dynamic Equilibrium and Repeatability

The typical recorded input and output signals from strain gages mounted on the bars in a SHPB test are plotted in Figure 4.3. Also plotted is the circumferential strain signal measured by the strain gage attached to a confinement sleeve. Initially, the incident pulse rises rapidly within 50  $\mu\text{s}$  duration time (rising-up phase), then increases slowly for about 450  $\mu\text{s}$  (loading phase), and then decreases in about 100  $\mu\text{s}$  (unloading phase). The transmitted pulse and circumferential strain signal have nearly linear characteristic during loading; unloading occurs after reaching a peak.

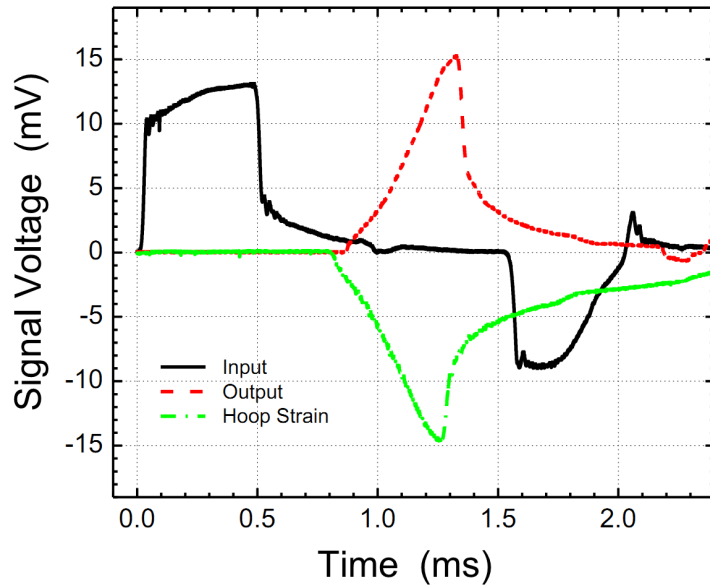


Figure 4.3: Oscilloscope recordings (Eglin sand initial density  $1.75 \text{ g/cm}^3$ ).

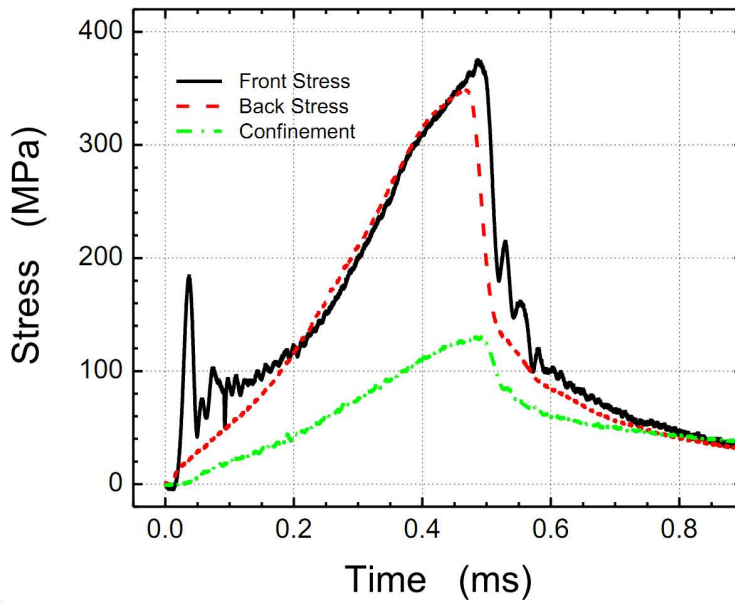


Figure 4.4: Dynamic stress equilibrium check.

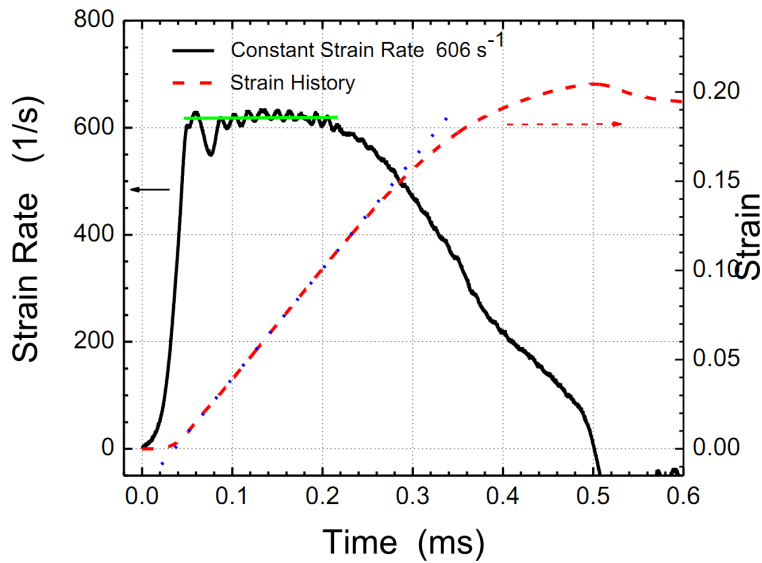


Figure 4.5: Strain rate and strain history.

In dynamic SHPB tests, when the stresses applied on both ends of the specimen are equal, the dynamic equilibrium state is established. Then the experiment is considered valid and the acquired experimental data are then processed to determine the stress - strain curves. To examine the dynamic equilibrium condition, the front stress and the back stress on the specimen were calculated following 1-wave, 2-wave method [33]. The stress at the front face (the end of specimen in contact with the incident bar) and back face (the end of specimen in contact with the transmission bar) is shown in Figure 4.4. The front stress was very close to the back stress during loading, indicating that the dynamic equilibrium condition was nearly established and the specimen was uniformly deformed. Figure 4.5 shows the strain rate and strain as a function of time. The nearly flat phase in strain rate history indicates that constant strain rate has been achieved. In a valid SHPB experiment, the incident, transmitted and reflected signals are processed further to determine the stress-strain relationship at high strain rates.

For the Eglin sand, we checked the experimental repeatability using the new sand assembly on SHPB. The resulting axial stress-axial strain curves were compared between sand specimens with controlled identical density while the testing condition was kept the same. The dynamic stress-strain curves

of dry sand with density  $1.51 \text{ g/cm}^3$  (uncompacted) and  $1.75 \text{ g/cm}^3$  (fully compacted) were shown in Figure 4.6(a) and 4.6(b), respectively. Results show well repeatability when the sand density was controlled. Higher density of sand ( $1.75 \text{ g/cm}^3$ ) showed better repeatable than the low density sand ( $1.51 \text{ g/cm}^3$ ).

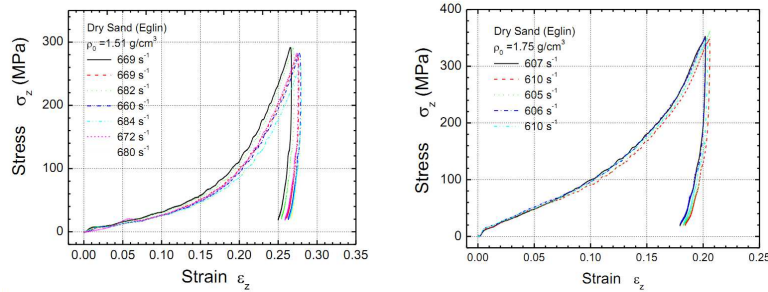


Figure 4.6: Reproducibility of SHPB test data. (a) Axial curve of sand with initial density  $1.51 \text{ g/cm}^3$ ; (b) Axial curve with density  $1.75 \text{ g/cm}^3$ .

### 4.1.3 Density Effects

For sand under confinement, the axial stress-axial strain curves (Figure 4.7(a)), hydrostatic pressure and volumetric strain curves (Figure 4.7(b)), 3D shear stress and shear strain curves (Figure 4.7(c)), were determined at high strain rates ( $600 \sim 700 \text{ s}^{-1}$ ). The error bar represents the standard deviation of eight experiments. In general, the axial stress-axial strain curve is linear at compressive strains from  $1 \sim 8\%$ , showing a trend similar to that reported in the literature cite Martin2009, Song2009. The slopes of these curves in the linear range are defined as apparent modulus  $E$  (ratio of axial stress to axial strain under confinement, Figure 4.7(a)). At compressive strains larger than 10%, the curves become steeper with increase in compressive strain. The stress-strain curves shift above with increase in initial mass density. The unloading curve shows an initial steep reduction in stress without recovery in deformation, followed by further reduction in stress with slight recovery in deformation. This is most likely because sand has been compacted, with its voids filled with fractured sand fragments, so that the sand sample behaves closer to a monolithic material. Similar trends

were found for volumetric response (Figure 4.7(b)) and deviatoric response (Figure 4.7(c)).

Results shown in Figure 4.7 indicate that both logarithmic isotropic and deviatoric stresses follow a two-segment linear relationship with strain, similar to the elastic and plastic behavior of metals. The linear range on a linear scale (Figure 4.7(a)) is similar to the transition regime between two linear segments in semi-logarithmic scale (Figures 4.7(b) and 4.7(c)). The first linear segment occurs most likely due to rearrangement of the sand grains with sliding and rotation, which can be referred to as sand grain-level elasticity, similar to the situation under quasi-static compression [25]. They all behave similarly at all densities in this segment. The second linear segment on a semi-logarithmic scale is perhaps associated with sand grain crushing, rearrangement of crushed fragments, and intact sand grains under higher pressure, which can be referred to as grain-level plasticity. The behavior in this region depends highly on the mass density. At higher initial mass density, the sand grains are closely packed. Hence, they provide high resistance for grain rearrangement, and consequently crushing becomes dominant. The shear behavior shows a yield-like step (Figure 4.7(c)), oscillating more at sand densities of 1.51 g/cm<sup>3</sup> and 1.63 g/cm<sup>3</sup>, than 1.75 g/cm<sup>3</sup>, which are also different from the smooth strain hardening in isotropic behavior (Figure 4.7(b)).

The three sets of loading curves in Figure 4.7, namely, axial stress-strain, volumetric behavior, and deviatoric response are found to follow a power law relationship with initial density, i.e.,  $\sigma \sim \rho_0^n$  (Figure 4.7). The exponent  $n$  was determined as 8.25, higher than 2~3 for foam [36, 38]. With the power law relation, the stress-strain curves of initial density 1.51 g/cm<sup>3</sup> can be scaled to determine curves at densities of 1.63 and 1.75 g/cm<sup>3</sup> (Figure 4.7). The scaled curves agree very well with the experimental curves. Table 4.8 gives a summary of the mechanical property data, including, apparent modulus, maximum stress reached, and maximum confinement pressure, as well as testing conditions, such as maximum confinement pressure reached.

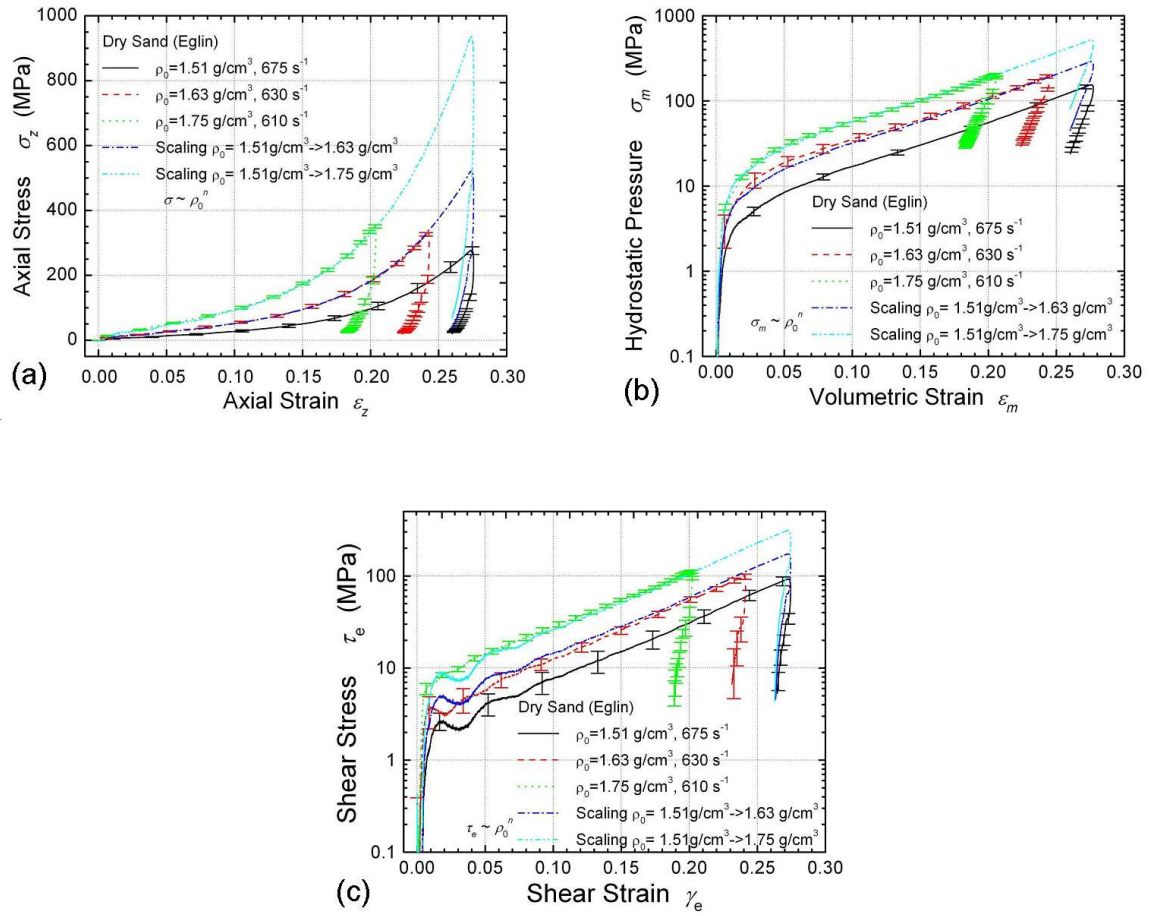


Figure 4.7: Multi-axial stress-strain curves of sand. (a) axial stress-strain curve; (b) hydrostatic pressure-volumetric strain curve; (c) shear stress-shear strain curve.

Notes:  $E$  is the apparent modulus, not the Young's modulus of sand as the sand is not under uniaxial stress state;  $K$  is the hydrostatic-pressure modulus;  $G$  is the shear modulus.

We next report the relationship between void ratio ( $e$ ) and axial stress (namely, pressure  $p$  in soil mechanics). Results on the  $e - \log p$  relationship have not yet been exploited in the literature at high strain rates. The void ratio is estimated using,  $e \approx \rho_s \frac{(1+\epsilon_z)}{\rho_0} - 1$ , where  $\rho_s$  is the skeletal density of sand and  $\rho_0$  is the initial bulk density. In a typical  $e - \log p$  plot, the axial compressive stress  $\sigma_z$  is taken as pressure  $p$ . Two linear segments appear in the  $e - \log p$  curve, representing a power law relationship

Figure 4.8: Properties of Dry (Eglin) Sand under Confinement (Density Effects).

Density $\rho$ (g/cm <sup>3</sup> )	Strain rate (s <sup>-1</sup> )	Apparent modulus			Maximum stress (MPa)	Maximum strain	Maximum Confinement (MPa)	$p_c$ (MPa)	$C_c$
		$E$	$K$	$G$					
1.51	675	236	157	77.8	277	27.4%	93.4±10.3	7.63	0.312
1.65	630	443	313	105	331	24.2%	131±11.8	15.7	0.303
1.75	610	848	520	217	352	20.2%	135±4.5	27.8	0.281

between  $e$  and  $p$ , similar to what is observed under quasi-static loading conditions [23, 62]. Two parameters, namely, preconsolidation pressure  $p_c$  (overburden pressure, namely, the transition pressure between two linear segments) and compression index  $C_c$  (magnitude of the slope in the linear segments of the  $e - \log p$  curve after preconsolidation) are determined and included in Table 4.8. The  $e - \log p$  curve during unloading also follows the linear relationship. At these high strain rates, with increase in the initial void ratio, the preconsolidation pressure decreases and the compression index increases.

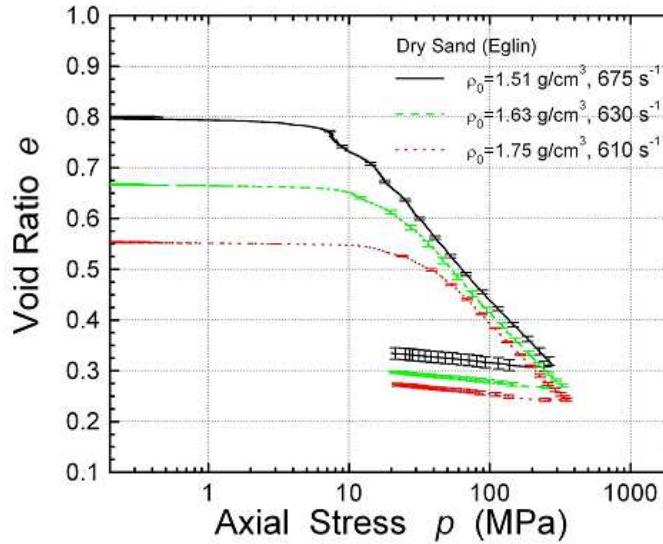


Figure 4.9:  $e - \log p$  curves of sand under confinement

We use Mohr-Coulomb relation to describe the shear stress  $\tau_e$  - hydrostatic pressure  $\sigma_m$  behaviors of sand. The Mohr-Coulomb relation is given as

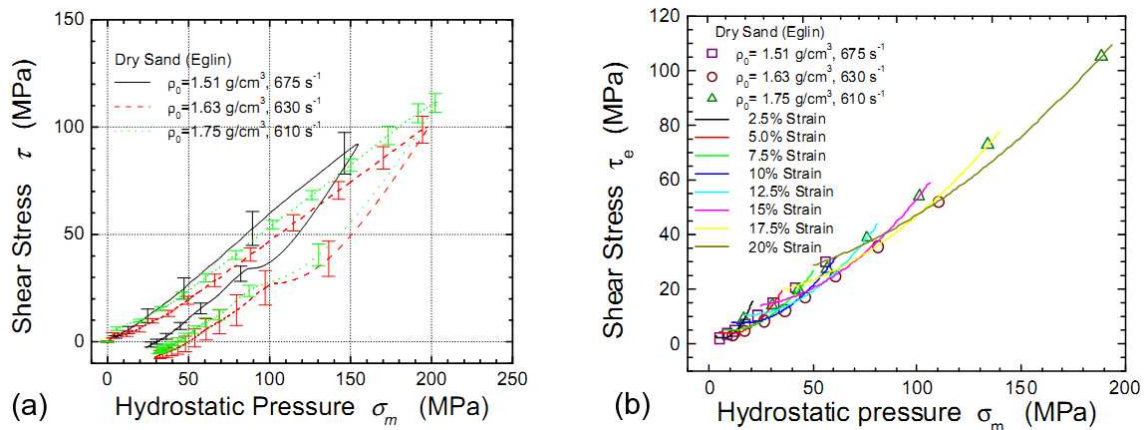


Figure 4.10: Mohr-Coulomb curves for dry Eglin sand. (a) Mohr-Coulomb curves; (b) Strain isolines in Mohr-Coulomb Curve

Table 4.1: Parameters in Mohr-Coulomb-relations.

Density $\rho$ (g/cm <sup>3</sup> )	Mohr A	Parameters b (MPa)
1.51	0.6656	-2.50
1.63	0.5599	-5.15
1.75	0.5961	-3.15

$\tau_e = a\sigma_m + b$ ; where  $a$  and  $b$  are constants. Figure 4.10(a) shows the Mohr-Coulomb relation during both loading and unloading for three sets of sand densities. At loading stage, the shear stress has the linear relationship with hydrostatic pressure. At unloading, it forms a hysteresis hoop, stiffer at first until the preconsolidation stress, and then follow the same trends as loading.

Figure 4.10(b) shows the strain isoline in Mohr-Coulomb curves from certain strain 2.5% to 20% data. With increasing strain, high shear stress and hydrostatic pressure, and lower slope of the curves. The parameters  $a$  and  $b$  for three sand densities are summarized into Table 4.1.

Figure 4.11(a) shows the SEM images of Eglin dry sand (as received) before SHPB impact test. The sand grains are irregular round or spherical in both large and small sizes. Figure 4.11(b) shows the SEM images of dry sand at density 1.75 g/cm<sup>3</sup> after SHPB impact test, which is loose and laid after disintegrated. The large sand grain had been peeled of Small fragments

were fractured from large sand grains forming powders.

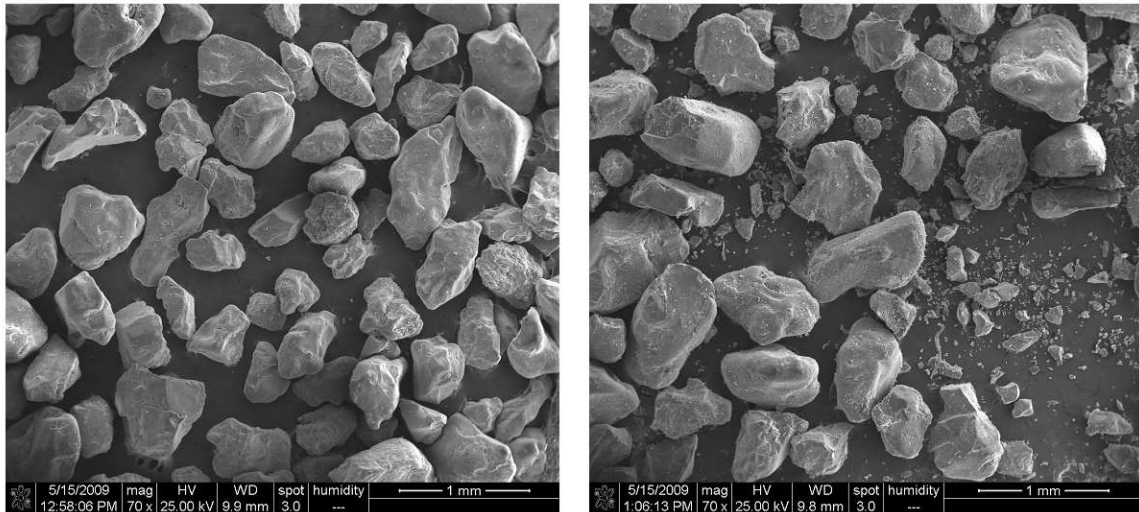


Figure 4.11: SEM images of as-received and impacted Eglin sand. (a) intact loose form as received; (b) after SHPB impact (initial density  $1.75 \text{ g/cm}^3$  with all sizes)

#### 4.1.4 Confinement Effects

A rigid confinement, such as that induced by aluminum and steel tubing, allows the sand specimen to deform in a nearly uniaxial strain state, while a soft confinement provided by PC and PVC tubing makes sand specimen to deform in a stress state closer to a uniaxial stress state. When the hollow cylinder passively confines a specimen, the confinement pressure can be calculated [39, 47] from  $p = 0.5(\alpha^2 - 1)\sigma_y$ ; where  $\alpha$  is the ratio of OD to ID of the tubing; and  $\sigma_y$  is the circumferential stress on the sleeve surface. If the sleeve is in elastic range,  $\sigma_y$  can be easily calculated by measuring the circumferential strain  $\epsilon_\theta$  using  $\sigma_y = E_c \epsilon_\theta$ , where  $E_c$  is Young's modulus of the tubing. When the tube yields, the calculation of confinement pressure 'p' is complex, but can be estimated as the dynamic yield stress  $\sigma_y$  of the tubing, which can be determined on SHPB experiment on tubing material under similar strain range.

From Figure 4.4(a), the confinement pressure by steel tubing changes with the axial strain, and is approximately proportional to the axial stress. The

maximum confinement pressure is 135 MPa. When aluminum tubing is used in confinement, the confinement pressure is lower than that induced by steel tubing. Since the maximum confinement pressure induced by steel tubing is 135 MPa in this work, the steel tubing is in the elastic regime. The aluminum tubing has a yield stress of 300 MPa under dynamic loading condition. Hence, it is also in the elastic range, since the maximum confinement pressure is estimated at 47.3 MPa. Using the measured dynamic yield stress, the maximum confinement pressures are estimated at 35.2 MPa for PC tubing, and 7.7 MPa for PVC tubing, respectively. The confinement pressure follows a nearly linear relationship with time in this work.

For sand under confinement, Figure 4.12 shows the axial stress-axial strain curves at different confinement pressures at high strain rates ( $600\sim 700\text{ s}^{-1}$ ). The error bar represents the standard deviation of the stress-strain curves. In general, the stress-strain curve behaves linearly at compressive strains of up to 11–13%, showing similar trend as reported [51], similar to Figure 4.7(a). The stress-strain curves are shifted higher gradually from confinements from PVC, PC, aluminum, and to steel sleeve, with increasing confinement pressure. The mechanical properties of sand under different confinements are summarized in Table 4.13.

Note, for hardened steel tubing, the inside wall surface confining sand was not indented by sand grain during SHPB testing, showing valid confinement calculation. However, for aluminum and plastic tubing (PC and PVC), the surface was indented by sand grain. So the confinement pressure was estimated according to yield strength of the tubing with possible linear relation with axial stress. Hence, the dynamic multi-axial compression behavior of sand can not be described by soft confining tubing but by hardened steel tubing.

#### 4.1.5 Moisture Effects

In the sand assembly preparation, specific amount of water was added into initial un-shaken sand to prepare moist sand using digital weighing scale. High vacuum grease was used to seal the gap between the WC rod and

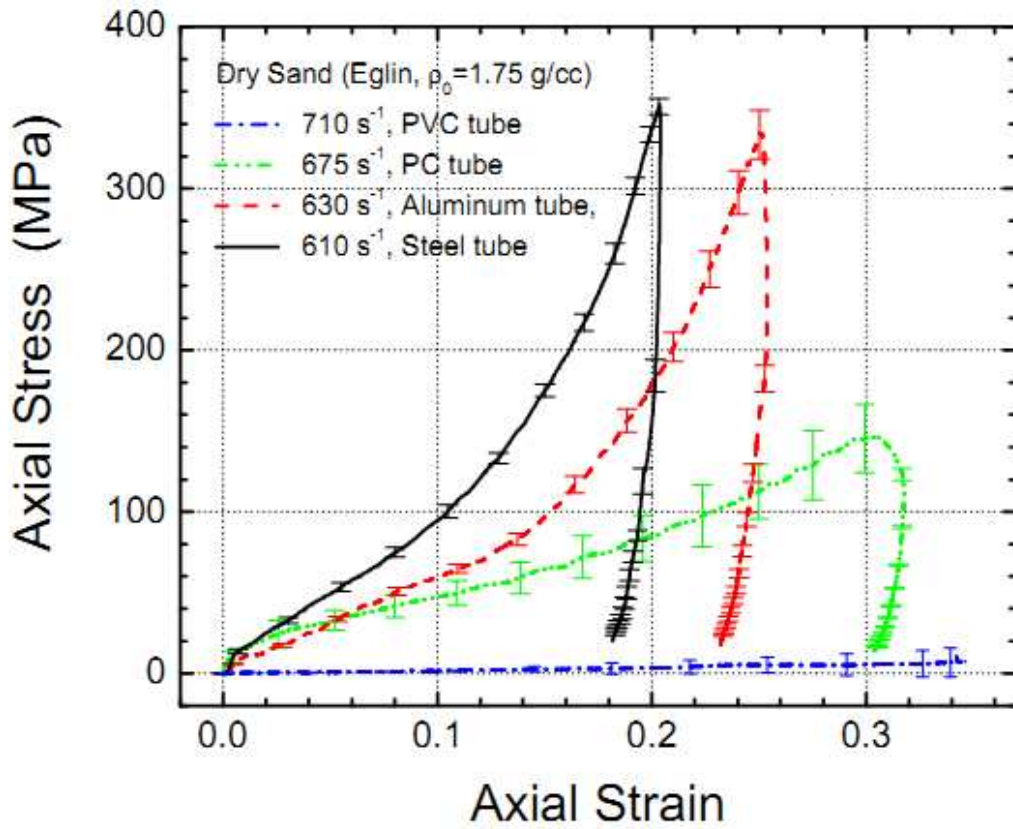


Figure 4.12: Axial Stress-Strain Curves (Effect of Confinement).

Figure 4.13: Mechanical Properties of sand under confinement (Confinement Effects).

Confinement Tubing	Density $\rho$ (g/cc)	Strain rate ( $s^{-1}$ )	Apparent modulus $E$ (MPa)	Maximum stress (MPa)	Maximum strain	Maximum Confinement (MPa)
Steel	1.51	675	236	277	27.4%	93.4±10.3
Steel	1.63	630	434	331	24.2%	131±12
Steel	1.75	610	848	352	20.2%	135±4.5
Aluminum	1.75	630	593	330	25.1%	47.3±1.6
PC	1.75	675	313	147	30.3%	35.2±1.4
PVC	1.75	710	20.3	6.7	22.8%	7.7±0.7

Note: Some properties of sand with steel confinement are repeated in Table1. ID 1/2" and OD 3/4" for steel and aluminum sleeve; OD 5/8" for PVC and PC sleeves

tubing inside surface to prevent water coming out during shaking. Then the sand assembly was shaken to form compact sand with moisture. Except the moisture, the density is controlled the same  $1.75 \text{ g/cm}^3$  as compact dry sand. Through shaking, water was evenly distributed into the gaps between the sand grains. Before and after shaking, the weighting scale is also used to monitor the weight of the whole assembly. Totally, 16.5% w/w maximum water can be added into the compact sand, corresponding to 80% saturation. For 4.2% w/w water, it corresponds to  $\sim 20\%$  moisture saturation. The SHPB results with 20% and 80% water saturation were compared with as received dry sand. Figures 4.14(a), 4.14(b), and 4.15(a) show the dynamic axial stress-axial strain, hydrostatic behavior, and deviatoric behavior with two moistures at strain rate  $\sim 600 \text{ s}^{-1}$ , respectively.

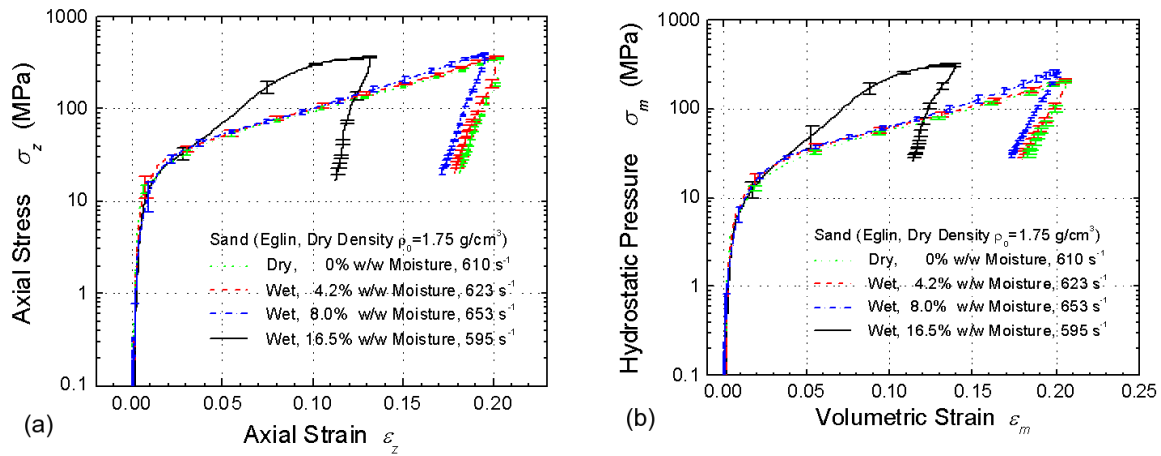


Figure 4.14: Dynamic stress-strain curves showing moisture effects. (a)  $\sigma_z - \epsilon_z$  in SHPB axial; (b)  $\sigma_m - \epsilon_m$  in dilatational behavior.

Figure 4.15(b) shows the Mohr-Coulomb relation with moisture effects. The lower content moisture (4.2% w/w) shows similar behavior as dry sand. However, highest moisture (16.5% w/w) shows stiffer behavior beyond the preconsolidation stress due to water incompressibility for both axial compression (Figure 4.14(a)) and hydrostatic behavior (Figure 4.14(b)). The shear behavior shows stiffer behavior at first after preconsolidation stress due to existing 20% air inclusion inside the sand sample and then it returns back showing that water can lubricate the contact surface between sand grains after water was filled fully between said grains. The shear stress

then behaves like a flow-like platen.

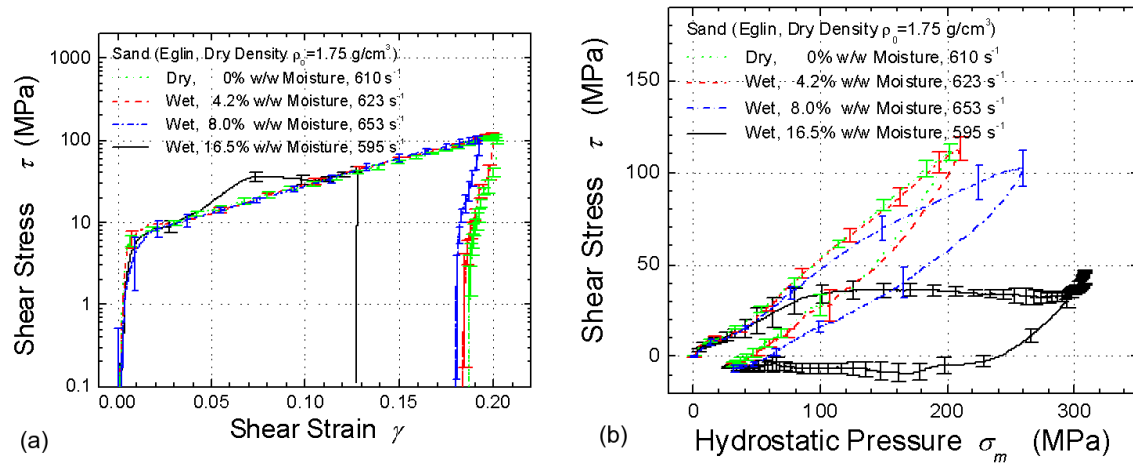


Figure 4.15: Dynamic stress-strain curves showing moisture effects. (a) 3D shear stress-strain curves; (b) Mohr-Coulomb Relation.

Figure 4.16(a) shows the  $e$ -log  $p$  curve of sand with moisture effects and Figure 4.16(b) shows the axial stress-bulk density with moisture effects. Notes, the 3-D  $\tau_e - \gamma_e$  is in  $45^\circ$  any plane of the axial  $z$ -direction. Since water is added, the bulk sand density was higher than the dry one. The density in Figure 4.16(b) was calculated from axial strain and the radial deformation can be ignored. After pre-consolidation, the slope of the axial stress-bulk density with 16.5% w/w moisture is higher than dry and low moisture sand.

## 4.2 Conclusions

In summary, we have investigated the dynamic compressive behavior of dry sand (Eglin) under confinement using a split Hopkinson pressure bar (SHPB) at high strain rates ( $600 \text{--} 700 \text{ s}^{-1}$ ). A technique was developed to prepare sand samples with consistent densities. Sand samples with three densities were compressed under high strain rates to determine both bulk and deviatoric responses. The curves of axial stress-axial strain, hydrostatic pressure-volumetric strain, 3D shear stress and shear strain of sand were determined up to 27% compressive strain at high strain rates. The  $e - \log p$  curve shows sand compressibility as a function of initial density. Significant density effects were identified and characterized with high accuracy. The stress-strain relationships follow a power law relationship

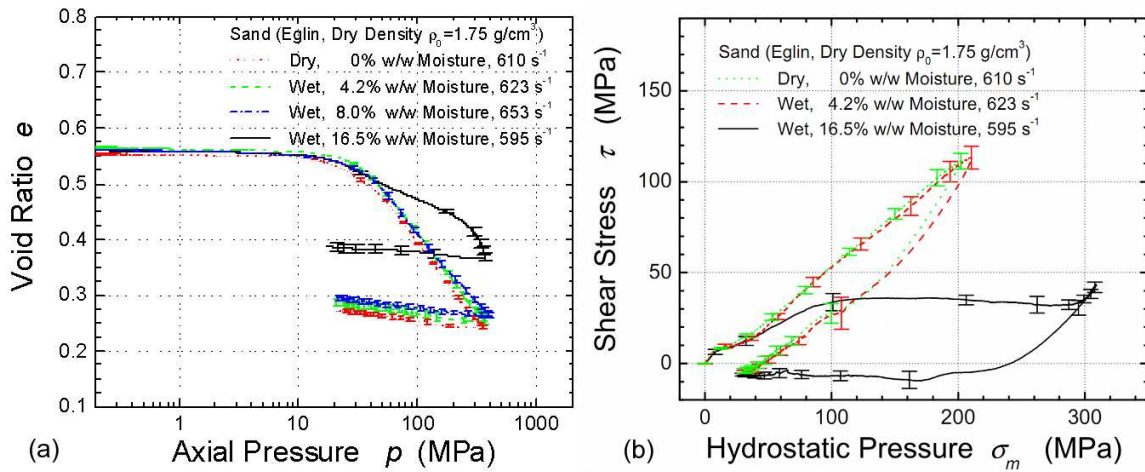


Figure 4.16: Dynamic stress-strain curves showing moisture effects. (a). Void ratio relation with axial pressure:  $e \log p$  curve; (b) axial stress-density curves.

with mass density and the exponent is determined as 8.25, an extremely high value indicating triaxial mechanical behavior highly sensitive to initial mass density. Moisture has small effects under low moisture concentration (<20%) but has a very strong effect at higher concentration (80%). Mohr-Coulomb relation shows slight changes for density effect, significant for saturated sand. Dynamic behavior of sand depends on the magnitude of confined pressure induced by tubing. These results can be analyzed further for constitutive modeling and for mesoscale simulations to quantify the dynamics of sand under high pressure and high rate deformation.

## Chapter 5

# Micro-computed Tomography

*This work was conducted by Praful Bari, Hrishikesh Bale, Rutuparna Narulkar and Jay Hanan of Oklahoma State University. The details of this work are documented elsewhere [5].*

Deformation of sand have been investigated by Desrues et al. [18], Tani [54] and others [45, 59] using X-ray Computed Tomography (CT). Otani *et al.* [45] developed a triaxial test apparatus to characterize the progressive failure with strain localization in sand during in-situ X-ray computed tomography. These experiments investigated the mechanism of failure through multi-axial compression. In-situ information on sand failure behavior is limited from these tests as the focus was mainly on modeling and ex-situ failure analysis. The experiments reported here investigate the in-situ failure behavior of sand through X-ray tomography. Experiments were conducted at the Advanced Photon Source (APS), Illinois, USA. Moreover, through this experiment some prior models and data have been validated. X-ray Computed Tomography was used to study strain localization, shear band formation, and deformation of sand grains by direct observation of internal structure of sand while it deforms under applied load.

A custom compression test fixture was developed to carry out these experiments which characterize sand failure by taking into consideration the mechanical properties and the influence of applied stresses on near and far-field regions. Eglin sand, with average grain size of 420  $\mu\text{m}$ , were enclosed in a polycarbonate tubing, shown in figure 5.1, with inner diameter

of 2.38 mm and wall thickness of 2.27 mm. Hardened tool steel discs were used as upper and lower platens. A custom screw driven load frame by Hanan *et al.* [26] was used to apply the compressive load (maximum limit of 622 N) on the sand samples during X-ray tomography and X-ray diffraction tests. Figure 5.2 shows the schematic of the  $\mu$ -CT setup at the APS 2-BM facility. Monochromatic X-ray beams with average energy of 23.8 keV was used. A complete scan of each section was taken at different equally spaced 280 ms exposures through 180°, capturing 1442 images. The voxel size was  $1.45 \times 1.45 \times 1.45 \mu\text{m}^3$ . After reconstruction, the size of each tomography slice was 16 MB. A total of 63 tomograph sets were obtained between 0% and 34% axial strains. The tomographs were further processed to reduce the huge size of the raw data and to reduce the noise due to the high resolution of the images. Amira was used for 3D visualization of the tomographs.

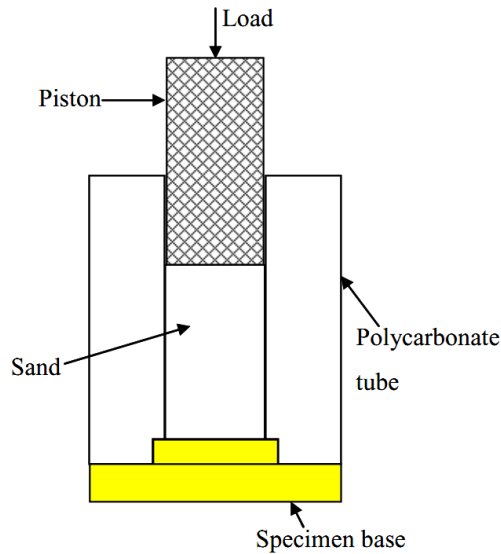


Figure 5.1: Vertical cross section of confinement of assembled compression testing system and sand specimen.

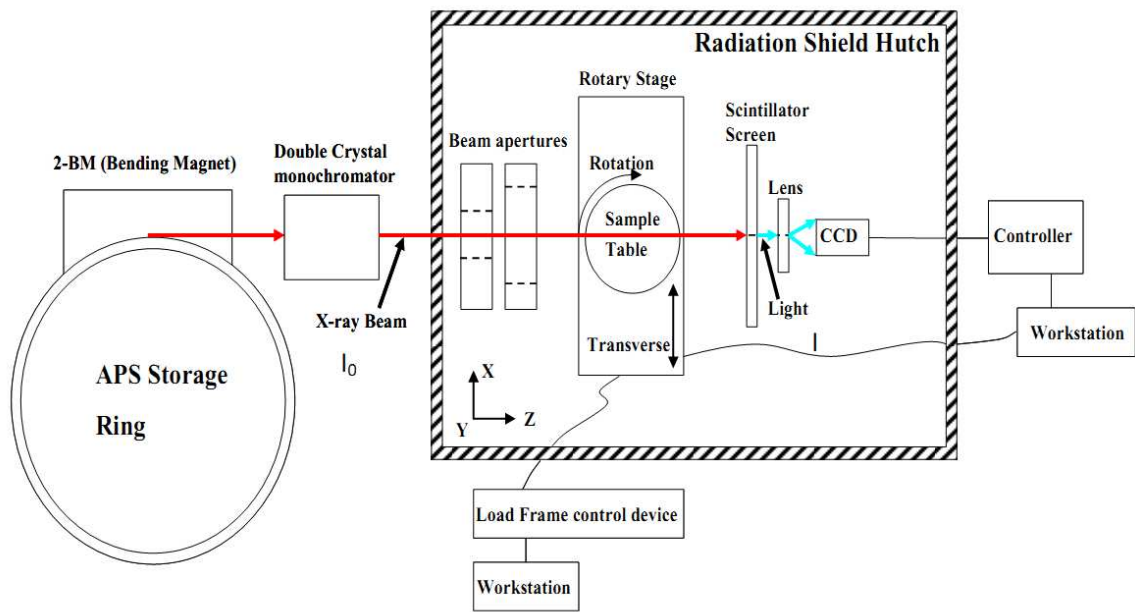


Figure 5.2: Diagram of the X-ray  $\mu$ -tomography beamline at the Advance Photo Source 2-BM.

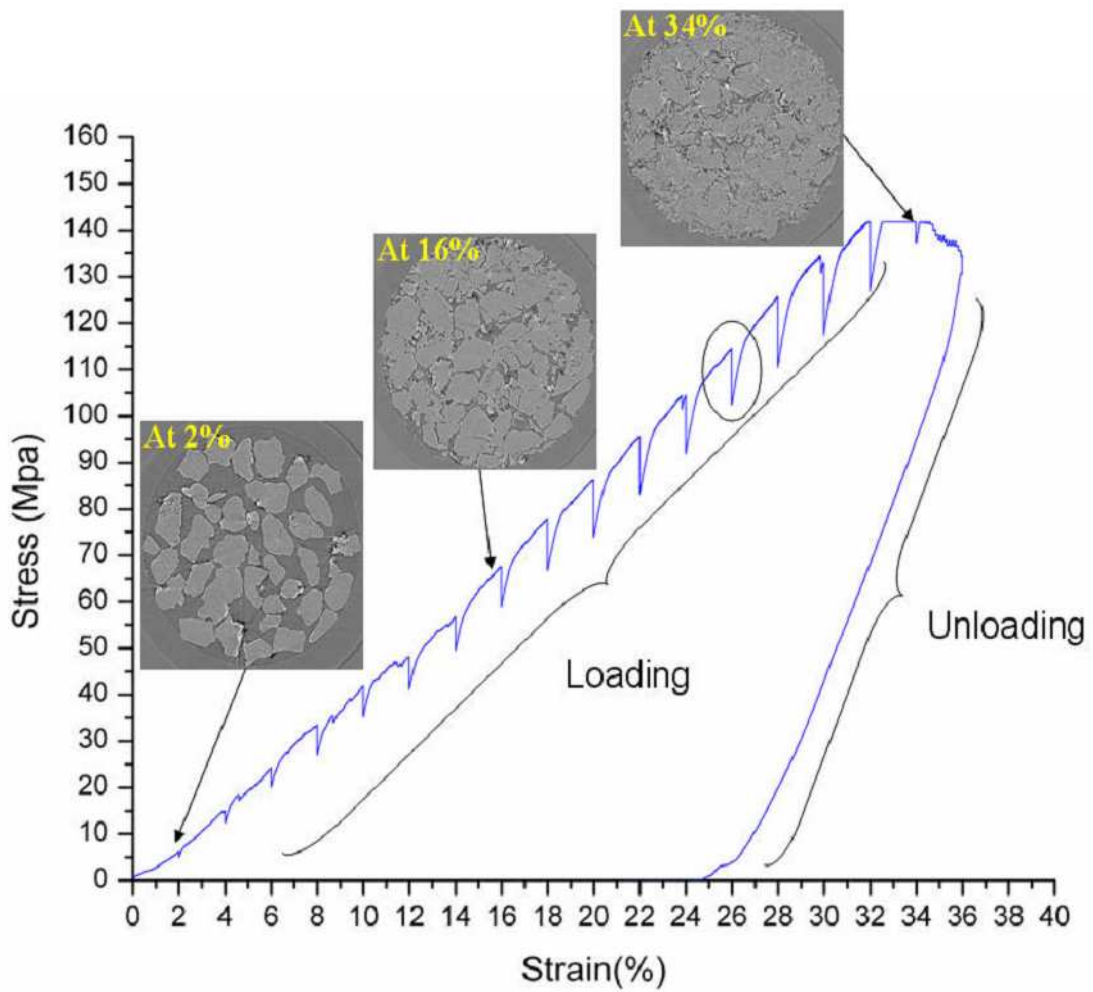


Figure 5.3: Axial stress vs axial strain response of Eglin sand under compression showing loading and unloading response segments. The loading was held at discrete axial strains for  $\mu$ CT imaging, causing drops in the axial stress due to relaxation of the load frame as seen in the loading segment.

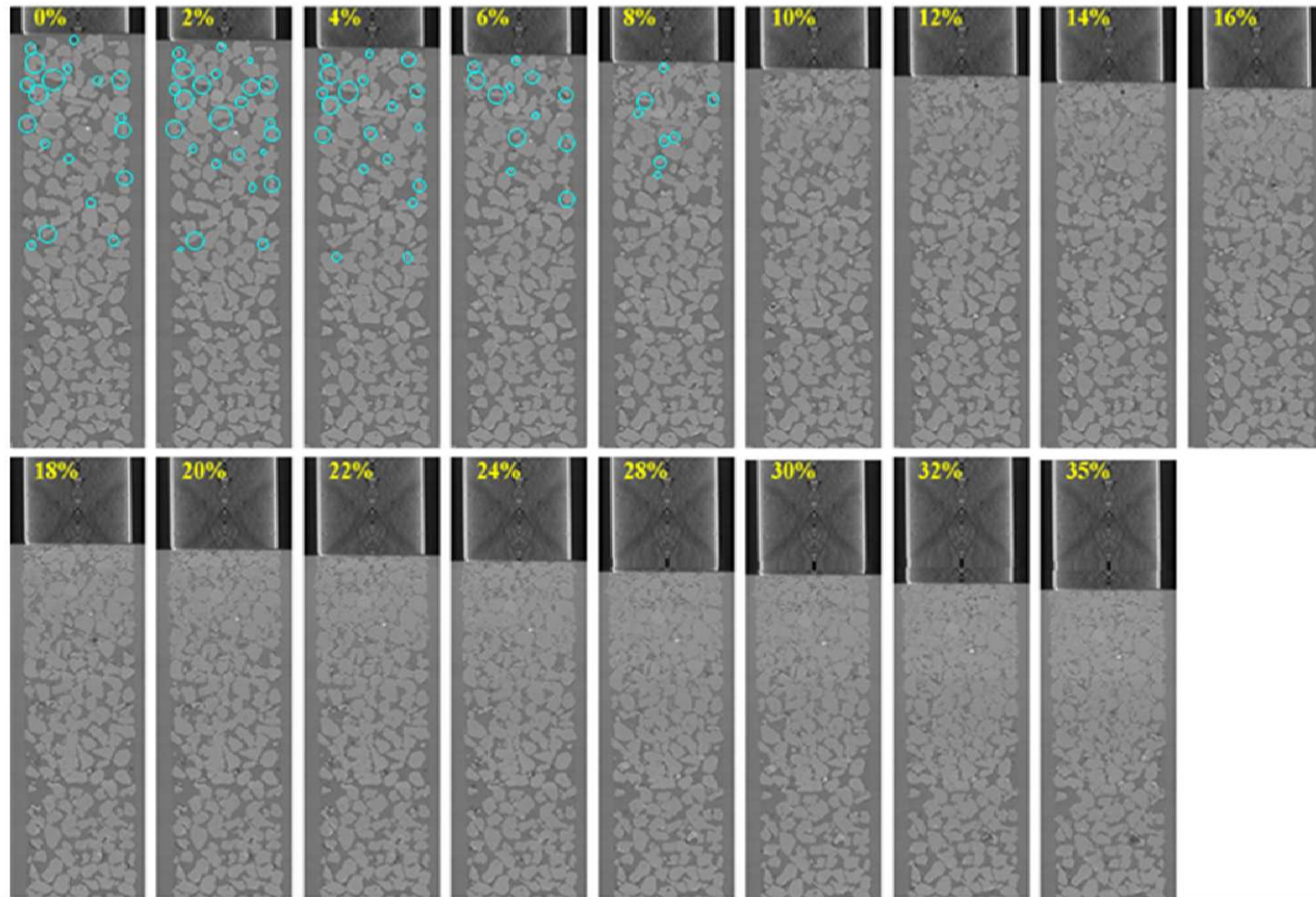


Figure 5.4: 2D reconstructed central cross-section slices of Eglin sand under compression from axial strains of 0% to 35%.

Table 5.1: Crack initiation stress with corresponding particle size for Eglin sand.

Particle Size (mm)	Crack Initiation Stress (MPa)
0.40 - 0.50	20
0.20 - 0.30	36
0.10 - 0.15	60
0.02 - 0.06	94

Figure 5.4 shows the cross-section slice of the Eglin sand grains during compression. At 2% strain reorientation of sand grains begin and their count progressively decreases with each increasing strain step. Beyond 10% strain, which approximately correspond to the break point stress value, reorientation of grains is almost zero and only fragmentation continues. At 30-40 MPa, significant crumbling of grains was seen. The loading curve has a polynomial fit and a gradual decrease in specific volume is observed with increasing stress. Further detailed micro structural observations show that failure of sand grains was highly localized. It has to be noted that the grains in the encircled region of the central slices corresponding to different strain values have translated or rotated in the immediate next image corresponding to the next strain step. This implies that with increasing strain rates, grains tend to move and resettle till a strain of 8%. Beyond 6% axial strain, resettling lessened. After 10% axial strain, crushing became predominant, and resettling was negligible. The smaller the particle size, the higher the load bearing capacity. Based on this, it is seen that at high strain, the grains in the near-field region undergo fragmentation, become smaller and start taking up more load. This results in very little load transfer to the grains in the far-field region and their subsequent resettling.

Table 5.1 relates the particle size range to the corresponding crack initiating stress and the analogous strain percentage. Bigger grains with larger surface areas begin to break at lower stress levels than the smaller grains. This is because the bigger grains are in contact with more number of grains than the smaller ones, and so the contact stresses acting on them is higher. It should be noted that, for big grains of the same size, the local crack initiating stress need not be the same and the far-field stress is lower for the large grain being

subjected to higher contact stresses. In general, larger the particle, lower is the far field crack initiating stress.

# Bibliography

- [1] Standard practice for classification of soils for engineering purposes (Unified Soil Classification System), 2001. Section 4, Volume 04.08. [page 5]
- [2] W.A. Allen, E.B. Mayfield, and H.L. Morrison. Dynamics of a projectile penetrating sand. *Journal of Applied Physics*, 28(3):370–376, 1957. [page 29, 30]
- [3] W.A. Allen, E.B. Mayfield, and H.L. Morrison. Dynamics of a projectile penetrating sand. Part II. *Journal of Applied Physics*, 28(11):1331–1335, 1957. [page 29, 30]
- [4] J.R. Arthur and B.K. Menzies. Inherent anisotropy in a sand. *Geotechnique*, 22(1):115–128, 1972. [page 4]
- [5] P. Bari. X-ray computed tomography of mechanical deformation in sand under compression. Master’s thesis, Oklahoma State University, 2010. [page 69]
- [6] A.K. Bhattacharya and W.D. Nix. Finite element simulation of indentation experiments. *International Journal of Solids and Structures*, 24(9):881 – 891, 1988. [page 21]
- [7] A.K. Bhattacharya and W.D. Nix. Finite element analysis of cone indentation. *International Journal of Solids and Structures*, 27(8):1047 – 1058, 1991. [page 21]
- [8] A. Bolshakov and G. M. Pharr. Influences of pileup on the measurement of mechanical properties by load and depth sensing indentation techniques. *Journal of Materials Research*, 13:1049–1058, 1998. [page 27]

- [9] J.P. Borg and T.J. Vogler. Mesoscale simulations of a dart penetrating sand. *International Journal of Impact Engineering*, 35:1435–1440, 2008. [page 29]
- [10] A. Bragov, G. Grushevsky, and A. Lomunov. Use of the Kolsky method for confined tests of soft soils. *Experimental Mechanics*, 36(3):237–242, 1996. 10.1007/BF02318013. [page 51]
- [11] A.M. Bragov, A.K. Lomunov, I.V. Sergeichev, K. Tsembelis, and W.G. Proud. Determination of physicommechanical properties of soft soils from medium to high strain rates. *International Journal of Impact Engineering*, 35(9):967 – 976, 2008. [page 51]
- [12] E. Calderon, M. Gauthier, F. Decremps, G. Hamel, G. Syfosse, and A. Polian. Complete determination of the elastic moduli of  $\alpha$ -quartz under hydrostatic pressure up to 1 GPa: an ultrasonic study. *Journal of Physics: Condensed Matter*, 19:1–13, 2007. [page 16]
- [13] W.A. Charlie, C.A. Ross, and S.J. Pierce. Split-Hopkinson pressure bar testing of unsaturated sand. *Geotechnical Testing Journal*, 13(4):291–300, 1990. [page 51]
- [14] S. Chocron, J.D. Walker, A.E. Nicholls, A.K. Dannemann, and C.E. Anderson Jr. Analytical model of the confined compression test used to characterize brittle materials. *Journal of Applied Mechanics*, 75(2):1–7, 2008. [page 35]
- [15] K.A. Dannemann, A.E. Nicholls, S. Chocron, J.D. Walker, and C.E. Anderson Jr. Compression testing and response of SiC n-ceramics: Intact, damaged and powder. In *Ceramic Engineering and Science Proceedings, Advances in Ceramic Armor, 29th International Conference on Advanced Ceramics and Composites*, volume 26, pages 109–116, 2005. [page 35]
- [16] M. Dao, N. Chollacoop, K.J. Van Vliet, T.A. Venkatesh, and S. Suresh. Computational modeling of the forward and reverse problems in instrumented sharp indentation. *Acta Materialia*, 49(19):3899 – 3918, 2001. [page 27]

- [17] N. Daphalapurkar, F. Wang, B. Fu, H. Lu, and R. Komanduri. Determination of mechanical properties of sand grains by nanoindentation. *Experimental Mechanics*, pages 1–10, 2010. 10.1007/s11340-010-9373-z. [page 4, 11, 46]
- [18] J. Desrues, R. Chambon, M. Mokni, and F. Mazerolle. Void ratio evolution inside shear bands in triaxial sand specimens studied by computed tomography. *Geotechnique*, 46(3):529–546, SEP 1996. [page 69]
- [19] J. Desrues, J. Lanier, and P. Stutz. Localization of the deformation in tests on sand sample. *Engineering Fracture Mechanics*, 21(4):909 – 921, 1985. [page 4]
- [20] C.W. Felice, E.S. Gaffney, J.A. Brown, and J.M. Olsen. Dynamic high stress experiments on soil. *Geotechnical Testing Journal*, 10(4):192–202, 1987. [page 51]
- [21] P. Forquin, A. Arias, and R. Zaera. An experimental method of measuring the confined compression strength of geomaterials. *International Journal of Solids and Structures*, 44(13):4291–4317, 2007. [page 35]
- [22] J. Geng, D. Howell, E. Longhi, R.P. Behringer, G. Reydellet, L. Vanel, E. Clement, and S. Luding. Footprints in sand: The response of a granular material to local perturbations. *Phys. Rev. Lett.*, 87:035506, Jul 2001. [page 4]
- [23] J. Graham, M. Alfaro, and Ferris; G. Compression and strength of dense sand at high pressures and elevated temperatures. *Canadian Geotechnical Journal*, 41:1206–1212(7), 2004. [page 3, 30, 50, 61]
- [24] G.T. Gray. *Classic split-Hopkinson pressure bar technique*, volume 8. Mechanical Testing and Evaluation, 2000. [page 54]
- [25] M.M. Hagerty, D.R. Hite, C.R. Ullrich, and D.J. Hagerty. One-dimensional high-pressure compression of granular media. *Journal of Geotechnical Engineering*, 119(1):1–18, 1993. [page 31, 45, 46, 47, 59]

- [26] J. Hanan, H. Bale, and N.B. Phelps. Materials tester for in-situ determination of mechanical and fatigue properties using x-ray radiation, Patent Application. [page 70]
- [27] E. Hanina, D. Rittel, and Z. Rosenberg. Pressure sensitivity of adiabatic shear banding in metals. *Applied Physics Letters*, 90:3, 2007. [page 34]
- [28] R.M. Haythornthwaite. Simple shear in granular media. *Applied Mechanics Reviews*, 50(11S):S81–S86, 1997. [page 4]
- [29] A.J. Hendron. *Behavior of sand in one-dimensional compression*. PhD thesis, University of Illinois, Urbana, Illinois, 1963. [page 30, 45]
- [30] J. Henrych. *The dynamics of explosion and its use*. Elsevier Scientific Publishing Company, Amsterdam, 1979. [page 30]
- [31] H.M. Jaeger, S.R. Nagel, and R.P. Behringer. The physics of granular materials. *Physics Today*, pages 32–38, 1996. [page 3, 29]
- [32] P.V. Lade and J.M. Duncan. Cubical triaxial tests on cohesionless soil. *Journal of the Soil Mechanics and Foundations Division*, 99(10):793–812, 1973. [page 4]
- [33] H. Lu, H. Luo, and R. Komaduri. Dynamic compressive response of sand under confinements. In *2009 SEM 2009 Annual Conference & Exposition on Experimental & Applied Mechanics*, June 1-4 2009. [page 53, 57]
- [34] H. Luo and W. Chen. Dynamic compressive response of intact and damaged AD995 alumina. *International Journal of Applied Ceramic Technology*, 1(3):254–260, 2004. [page 51, 54]
- [35] H. Luo, W. Chen, and A. M. Rajendran. Dynamic compressive response of damaged and interlocked SiC-N ceramics. *Journal of the American Ceramic Society*, 89(1):266–273, 2006. [page 54]
- [36] H. Luo, G. Churu, E. Fabrizio, J. Schnobrich, A. Hobbs, A. Dass, S. Mulik, Y. Zhang, B. Grady, A. Capecehatro, C. Sotiriou-Leventis,

- H. Lu, and N. Leventis. Synthesis and characterization of the physical, chemical and mechanical properties of isocyanate-crosslinked vanadia aerogels. *Journal of Sol-Gel Science and Technology*, 48:113–134, 2008. 10.1007/s10971-008-1788-y. [page [51](#), [53](#), [54](#), [59](#)]
- [37] H. Luo, H. Lu, W. Cooper, and R. Komanduri. Effect of mass density on the compressive behavior of dry sand under confinement at high strain rates. *Experimental Mechanics*, pages 1–12, 2011. [page [33](#), [50](#)]
- [38] H. Luo, H. Lu, and N. Leventis. The compressive behavior of isocyanate-crosslinked silica aerogel at high strain rates. *Mechanics of Time-Dependent Materials*, 10:83–111, 2006. 10.1007/s11043-006-9015-0. [page [51](#), [53](#), [54](#), [59](#)]
- [39] Z. Ma and K. Ravi-Chandar. Confined compression: A stable homogeneous deformation for constitutive characterization. *Experimental Mechanics*, 40(1):38–45, 2000. [page [33](#), [34](#), [54](#), [63](#)]
- [40] B.E. Martin, W. Chen, Bo Song, and S. Akers. Moisture effects on the high strain-rate behavior of sand. *Mechanics of Materials*, 41:786–798, 2009. [page [32](#), [48](#), [51](#)]
- [41] D.J. Murphy. *Stress, degradation, and shear strength of granular material*. Gulf Publishing Company, Houston, Texas, 1987. [page [30](#)]
- [42] M. Oda, J. Konishi, and S. Nemat-Nasser. Some experimentally based fundamental results on the mechanical behaviour of granular materials. *Geotechnique*, 30(4):479–495, 1980. [page [4](#)]
- [43] W.C. Oliver, R. Hutchings, and J.B. Pethica. Measurement of hardness at indentation depths as low as 20 nanometres, 1986. [page [27](#)]
- [44] W.C. Oliver and G.M. Pharr. An improved technique for determining hardness and elastic modulus using load and displacement sensing indentation experiments. *Journal of Materials Research*, 7:1564–1583, 1992. [page [27](#)]

- [45] J. Otani, T. Mukunoki, and Y. Obara. Characterization of failure in sand under triaxial compression using an industrial x-ray CT scanner. *International Journal of Physical Modelling in Geotechnics*, 2(1):15–22, 2002. [page 69]
- [46] H B Poorooshab, I Holubec, and A N Sherbourne. Yielding and flow of sand in triaxial compression: Part i. *Canadian Geotechnical Journal*, 3(4):179–190, 1966. [page 4]
- [47] K. Ravi-Chandar and Z. Ma. Inelastic deformation in polymers under multiaxial compression. *Mechanics of Time-Dependent Materials*, 4(4):333–357, 2000. [page 34, 35, 63]
- [48] D. Rittel, E. Hanina, and G. Ravichandran. A note on the direct determination of the confining pressure of cylindrical specimens. *Experimental Mechanics*, 48(3):375–377, 2008. [page 34]
- [49] C.A. Ross, P.T. Nash, and G.J. Friesenhahn. *Pressure Waves in Soils Using a Split-Hopkinson Pressure Bar*. Defense Technical Information Center, 1986. [page 51]
- [50] S. Shim, J. Jang, and G.M. Pharr. Extraction of flow properties of single-crystal silicon carbide by nanoindentation and finite-element simulation. *Acta Materialia*, 56(15):3824 – 3832, 2008. [page 22]
- [51] B. Song, W. Chen, and V. Luk. Impact compressive response of dry sand. *Mechanics of Materials*, 41(6):777 – 785, 2009. Advances in the Dynamics of Granular Materials. [page 51, 64]
- [52] V. Subramanian. Quasi-static compression of granular materials (Sand) at high pressures ( $\sim 3$  GPa). Master’s thesis, Oklahoma State University, 2010. [page 29, 36, 38]
- [53] D. Tabor. *The hardness of metals*. Monographs on the physics and chemistry of materials. Clarendon Press, 1951. [page 22]
- [54] S. Tani. *Deformation and progressive failure in geomechanics*. Pergamon, 1997. [page 69]

- [55] K. Terzaghi, R.B. Peck, and G. Mesri. *Soild mechanics in engineering practice*. John Wiley & Sons Inc., 3rd edition, 1996. [page 30]
- [56] S. Timoshenko and J.N. Goodier. *Theory of Elasticity*. McGraw-Hill, New York, 1951. [page 34]
- [57] A.S. Vesic and G.W. Clough. Behavior of granular materials under high stresses. *Journal of the Soil Mechanics and Foundations Division*, 94(3):661–668, 1968. [page 31]
- [58] G.E. Veyera. Uniaxial stress-strain behavior of unsaturated soils at high strain rates. Technical Report WL-TR-93-3523, Wright-Patterson Air Force base, 1994. [page 5, 6, 51]
- [59] G. Viggiani, N. Lenoir, P. Basuelle, M. Di Michiel, S. Marelllo, J. Desrues, and M. Kretschmer. X-ray microtomography for studying localized deformation in fine-grained geomaterials under triaxial compression. *Comptes Rendus Macanique*, 332(10):819 – 826, 2004. [page 69]
- [60] F. Wang, B. Fu, H. Luo, S. Staggs, R.A. Mirshams, W.L. Cooper, S.Y. Park, M.J. Kim, C. Hartley, H Lu, and R. Komanduri. Characterization of the mechanical properties of individual Eglin sand grains by nanoindentation. *Submitted to Mechanics of Materials*, 2011. [page 11]
- [61] Q. Wang and P.V. Lade. Shear banding in true triaxial tests and its effect on failure in sand. *Journal of Engineering Mechanics*, 127(8):754–761, 2001. [page 4]
- [62] J.A. Yamamuro, P.A. Bopp, and P.V. Lade. One-dimensional compression of sands at high pressures. *Journal of Geotechnical Engineering*, 122(2):147–154, 1996. [page 3, 30, 32, 47, 48, 50, 61]